International Journal of Petroleum Science and Technology
ISSN 0973-6328 Volume 17, Number 1 (2023), pp. 13-59

http://www.ripublication.com

Optimal Core Trip Velocity Ranges for Major US Shale Plays

**[1]Ali Taghichian, [2]Hamid Hashemolhosseini, [3*]Sayantan Ghosh,
[4]Musharraf Zaman, [5]Alireza Baghbanan and [6]Alireza Etedali**

*[1]Civil Engineering Department, Isfahan University of Technology, Iran
Email: taghichian@yahoo.com*

*[2]Associate Professor, Civil Engineering Department,
Isfahan University of Technology, Iran
Email: hamidh@iut.ac.ir*

[3,]Assistant Professor (Department of Petroleum Engineering)
Indian Institute of Technology (Indian School of Mines)
Dhanbad, JH- 826004, India
Corresponding Author Email: ghoshsayantan88@gmail.com
Phone: (+91)8420597611 ORCID ID: 0000-0002-1679-8833*

*[4]Professor, Civil Engineering and Environmental Science
University of Oklahoma. Norman, Oklahoma 73019, USA
Email: zaman@ou.edu*

*[5]Associate Professor, Mining Engineering Department,
Isfahan University of Technology, Iran
Email: bagh110@cc.iut.ac.ir*

*[6]Mining Engineering Department, Isfahan University of Technology, Iran
Email: eatedaly2000@yahoo.com*

Abstract

Many geomechanical and petrophysical reservoir properties are obtained via laboratory experiments. Safe core trip velocities from the reservoir to the surface during long trips are crucial to preserve the in-situ properties. This work demonstrates coupled porothermoelastic and thermoelastic simulations of six US shale plays to determine suitable velocities. Stress evolution substantially differs in our two simulation schemes (porothermoelastic and thermoelastic). Input properties for simulations were gathered from literature. This information was transformed into probabilistic distributions using the Monte Carlo random sampling technique and Voigt-Reuss-Hill averaging.

Three scenarios were defined, i.e., the most, the mean, and the least conservative. The estimated tripping velocities for the “most conservative” scenario lie between 0.18 m/s and 1.17 m/s for the Bakken Shale. The most conservative velocities for the other shale plays are in the range of 0.64-0.75 m/s. In the “mean” scenario, similar to the most conservative scenario, the least velocity was attributed to Eagle Ford at 1.21 m/s. No velocity limitations for the Bakken and Marcellus Shale plays were evident. Mean velocities for the remaining shale plays range between 1.3-1.84 m/s. For the “least conservative” scenario, only Haynesville Shale shows a limiting velocity of 1.79 m/s, while the others show no limiting velocities.

Keywords: Porothermoelastic, trip velocity, coring, unconventional, geomechanics

1. Introduction

During core tripping, the pressure and temperature of the core and accompanying fluids will drops from the reservoir to atmospheric conditions (Zubizarreta et al., 2011). Depending on the permeability value, the existing pore pressure may increase the tensile stress in the core. Surface core cooling increases tensile stress because it inhibits core expansion. These conditions can cause core damage and changes in fluid saturation, mechanical and poromechanical properties of reservoir rocks (Cornwall, 1990; Kneafsey et al., 2011).

To preempt such damages, some remedying approaches were created. For example, engineers created a pressure core tool that in principle controls the pressure of the reservoir by closing it in a pressurized chamber as it rises to the surface. This helps prevent damage to the core and fluid changes due to fluid removal and expansion. Saturation measurements of pressurized cores are also more reliable than measurements of conventional cores. However, they are still not 100% accurate, as pressurized cores can still be subjected to flushing while coring. Sponge core liners help in minimizing saturation measurement errors through retention of the expulsed formation fluids in a foam lining (Auman, 1986).

The gradual variation of pore pressure, temperature and temperature in the critical area will be studied in a combined porothermoelasticity (PTE) scenario. The porothermoelasticity theory predicts the behavior of rocks in systems containing porous and compressible body and liquids with some compressibility, each of which responds to temperature changes by expansion/contraction. In this case, water flow occurs due to the pore pressure gradient and thermal diffusion occurs due to heat conduction/convection. The birth of the theory dates back to 1923, when Terzaghi (1923) predicted the 1D consolidation of soil. Later, Biot (1941) developed a 3D coordinate system using Terzaghi's (1923) theory. Rice and Cleary (1976) redefine this theory in terms of the Skempton pore pressure coefficient (Skempton, 1954) and the wet (undrained) Poisson ratio. Palciauskas and Domenico (1982) and McTigue (1986) are also important in improving and developing the theory of porothermoelasticity.

Detournay and Cheng (1993) also provide a comprehensive review of the theory of development of poroelasticity.

The governing equations, i.e. laws of equilibrium, laws and laws of kinematics are as follows. Constitutive equations are shown in Eq. (1), which are Hooke, pressure, Darcy, and Fourier respectively:

$$\sigma_{ij} = 2G\varepsilon_{ij} + \left(\frac{2G\nu}{1-2\nu}\varepsilon - \alpha p - K\beta_s T\right)\delta_{ij} \tag{1a}$$

$$p = M(\zeta - \alpha\varepsilon + \beta T) \tag{1b}$$

$$q_i^f = -\kappa_{ij}^f\left(p_{,j} - f_j\right) \tag{1c}$$

$$q_i^T = -\kappa_{ij}^T T_{,j} \tag{1d}$$

The balance laws for momentum, mass, and energy, respectively are shown in Eqs. (2):

$$\sigma_{ij,j} + F_i = 0 \tag{2a}$$

$$\frac{\partial\zeta}{\partial t} + \nabla\cdot q^f = 0 \tag{2b}$$

$$\rho C_v\frac{\partial T}{\partial t} + \nabla\cdot q^T = 0 \tag{2c}$$

The kinematic relation is written as:

$$\varepsilon_{ij} = \frac{1}{2}\left(u_{i,j} + u_{j,i}\right) \tag{3}$$

in which σ, ε = total stress and strains, G, ν = rock moduli, p = pore pressure, T = temperature, δ_{ij} = Kronecker delta, K = dry bulk modulus, α = Biot pore pressure coefficient, β_s = expansion coefficient of the solid skeleton, F_i = solid body force, u = displacement, ζ = variation of fluid content, q_i^f = fluid flux, q_i^T = heat flux, $M = 2G(\nu_u - \nu)/[\alpha^2(1-2\nu_u)(1-2\nu)]$ is Biot modulus, f_i = fluid body force, κ^f = mobility of the fluid (rock permeability divided by fluid viscosity), κ^T = thermal conductivity of the porous rock, and β = undrained thermal expansion coefficient and is determined as $\beta = 3\left[(\alpha-\phi)\beta_s + \phi\beta_f\right]$ where β_f = fluid expansion coefficient. Under this convention, tensile stresses are considered positive.

Coupling of Eqs. (1-3) creates Navier type and diffusion equations, which can be written as follows:

$$Gu_{i,jj} + \frac{G}{1-2\nu}\varepsilon_{kk,i} - \alpha p_{,i} - K\beta_s T_{,i} + F_i = 0 \tag{4a}$$

$$\frac{1}{M}\frac{\partial p}{\partial t} - \frac{k_f}{\mu}p_{,ii} + \alpha\frac{\partial\varepsilon_{kk}}{\partial t} - \beta\frac{\partial T}{\partial t} + \kappa f_{i,i} = 0 \tag{4b}$$

The two mentioned field equations govern a PTE medium. Using these equations, in combination with relevant initial and boundary conditions, each field, i.e., pore pressure, stress, temperature, strain, and fluid content variation can be determined. To solve a PTE problem, the analytic approach is utilized in the case of simple geometries, having constant properties, and simple initial and boundary conditions. However, for complex geometries, having pressure-, stress-, and temperature-dependent properties, and challenging boundary conditions, numerical schemes are preferred in problem solving. Fast Lagrangian Analysis of Continua in three dimensions (FLAC3D) solves engineering mechanics computations through an explicit finite-difference program. It has the option of the coupled fluid-thermal-mechanical analyses (i.e., the mechanical response of a porous material may be studied under thermal diffusion and/or transient fluid flow) with sophisticated boundary conditions, complex geometries, and variability of input properties (FLAC3D manual, 2012).

Using realistic and physically plausible geomechanical data aids in the general understanding of the existing phenomena, as well as in obtaining reliable values towards infield practical applications. In this study, we performed a PTE simulation of core tripping for six US unconventional shales. These plays are Eagle Ford, Marcellus, Woodford, Haynesville, Barnett, and Bakken. In order to be able to propose acceptable velocity ranges for the six selected shales, a comprehensive literature survey and a detailed geomechanical characterization were performed. The conducted characterization study results in geomechanical characteristics, each with its own reliability, mean value (MV), and standard deviation (SD) depending upon the location, depth, and geological stratigraphy of the field where the core was obtained. Additionally, it results in the mean, the most conservative, and the least conservative scenarios by which one can obtain the range of tripping velocities for these shale plays.

2. Geological overview of the shale plays

The locations of the six shale plays, scattered within the north, south, and northeastern part of the lower 48 states of the United States of America are shown in Fig. 1. These six shale plays are the major contributors of U.S. onshore hydrocarbon production and have land operations by almost every major oil and gas giant.

The Marcellus Shale is one of the most prolific producing formations in the eastern United States (Fig. 1). It was deposited during the Middle Devonian time (~390 million years ago) in a foreland basin that is approximately parallel to the trend of the present-day Appalachian Mountains (Harper, 1999). Across the Appalachian Basin, the Marcellus Shale thickness decreases westward from the central part of the basin and pinches out in the subsurface towards the east. The formation thickness is nearly 900 feet in south-central New York and loses thickness to the south and east, varying in the range of 200-600 feet in northeastern Pennsylvania. Recent production has mostly taken place where the formation thickness is larger than 50 ft (U.S. EIA, 2017a). Some of the lithologies mentioned by previous authors include silty shale with enclosed pyrite, calcareous shale, and carbonate concretions (Ettensohn and Baron, 1981; Harper, 1999; Roen and Walker, 1996). Marcellus Shale is under-pressured in its southwestern portion and normal- to potentially over-pressured in its northeastern portion (Zagorski et al., 2012). He (2011) reported Marcellus Shale matrix permeability values in the range of 100-450 nd. Thermal maturity based on vitrinite reflectance ranges 0.5-3.5% and increases in the southeastern direction. Most of the production takes place in the western parts of West Virginia, Pennsylvania, eastern Ohio, and southern New York (U.S. EIA, 2017a). Annual natural gas production from the Marcellus in 2012 was greater than 2 TCF (Rowan et al., 2014). The annual production of natural gas liquids is approximately 2 million BBL (Wang and Carr, 2013).

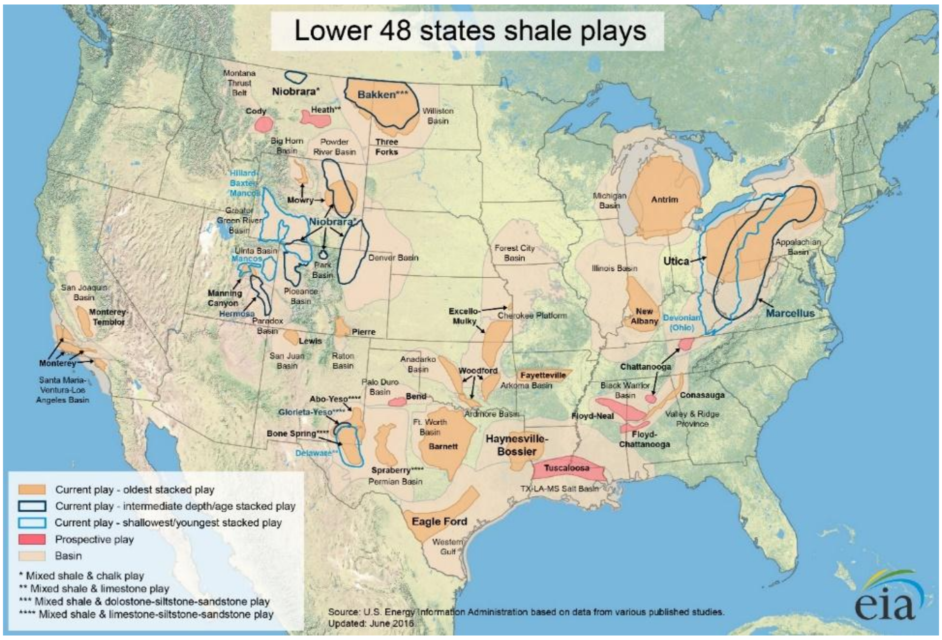

Source: U.S. Energy Information Administration based on data from various published studies.
Updated: June 2016

Figure 1. Shale plays in the United States (stars depict the locations of the six shale plays that are the focus of this study). Modified from EIA (2016)

The Woodford Shale is the most productive shale formation in the state of Oklahoma and covers a large portion of the state (Fig. 1). It was deposited during Upper Devonian-Lower Mississippian Time (Hass and Huddle, 1965). Prolific basins producing from the Woodford Shale include the Anadarko, Ardmore, and Arkoma Basins (Fig. 1). Woodford Shale is highly fractured/jointed (Ghosh et al., 2018a; Ghosh and Slatt, 2019) and often observed in the outcrop in alternating brittle and ductile (or hard and soft) beds (e.g., Galvis-Portilla, 2017; Ghosh, 2017). The Main mineral constituents of the Woodford Shale are quartz, followed by clay and dolomite (e.g., Becerra-Rondon, 2017; Ghosh et al., 2018a; Ghosh et al., 2018b). “According to the annual IHS database (2016), cumulative production from 2004 to 2015 was 56.4 MMBO and 3.9 TCFG” (Dewers et al., 2019, p. 165). Total thickness ranges from near zero to about 125 ft (40 m) on the shelf areas of Northern Oklahoma to greater than 900 ft (270 m) in some parts of the Anadarko Basin (Amsden, 1975). Curtis et al. (2012) reported a thermal maturity range of 0.51% Ro to 6.36% Ro. According to Slatt et al. (2012), the Woodford Shale contains type II kerogen, which is indicative of a marine environment of deposition.

The Mississippian-age Barnett Shale is known as the primary hydrocarbon source rock of the Paleozoic conventional reservoirs in the Fort Worth Basin (Pollastro et al., 2004; Montgomery et al., 2005) which is shown in Fig. 1. The Barnett Shale thermal maturity ranges from 0.7 to 1.7% (Montgomery et al., 2005). Cluff et al. (2007) reported an average matrix permeability of 100 nd. The Barnett Shale in the Fort Worth Basin covers an area with 38 counties in north-central Texas (Jarvie et al., 2007). The Newark East Barnett Shale Field in the Fort Worth Basin of North Texas is now the largest gas field within Texas. This shale holds greater than 140 BCF per square mile of gas in place. As of 2012, the Newark East field, the largest gas field in the state of Texas, was producing more than 800 MMCF per day (Hall, 2004).

The Upper Jurassic Haynesville is a unique and highly prolific shale play located in northwest Louisiana and east Texas (Fig. 1). The Haynesville Shale is highly over-pressured (0.8 to greater than 0.95 psi/ft pore pressure gradient) (Wang and Hammes, 2010), which makes it unique compared to other shales. This overpressure makes the wells highly productive. The cumulative dry gas production from 2004 to mid-2019 was ~18.4 TCF (Milkov et al., 2020). The Haynesville Shale in the northwest parts is siliciclastic and clay rich; carbonate content and TOC increase towards the west and south (Buller and Dix, 2009; Spain and Anderson, 2010). The Haynesville Shale, which is matrix-porosity dominated (Wang and Hammes, 2010) and mechanically weak (Buller, 2010) stands in stark contrast to the organic-porosity-dominated and mechanically strong Barnett Shale (North Texas). The average porosity of the Haynesville Shale is ~11%, which is relatively high compared to other shale plays (Wang and Hammes, 2013). Production from the Haynesville is dependent upon pore pressure gradient, effective stress, reservoir quality, and completion practices (Wang and Hammes, 2013). The Pressure gradient increases from the north (shallow) to the east and southeast (deep). Following the same north to south trend, clay content decreases, TOC increases from 1.75 to 3.75%, thermal maturity (Ro) increases from 1.25 to 2.25%. (Buller and Dix, 2009; Dix et al., 2010; Spain and Anderson, 2010; Younes et al., 2011).

The Eagle Ford Group is an Upper Cretaceous formation in the Gulf Coast basin of southern Texas. The Eagle Ford is a source rock for other Cretaceous reservoirs such as the Buda and Austin chalk. It has thermal maturities approximately in the range of 0.7-1.3%. Stoneburner (2017) reported calcite, followed by quartz, clay minerals, and feldspar as the major mineral constituents. As of December 2014, the Eagle Ford in the Gulf Coast basin had cumulative production of nearly 1.1 billion BBL of oil and condensates and 4.8 trillion cubic ft of natural gas (TCFG). On average, in 2014 it produced approximately 4.9 billion cubic ft of natural gas per day (BCFGD) and 1.3 million BBL of oil and condensate per day. The entire resource potential of the Eagle Ford, even though subjective, has been estimated to be 25- 30 billion BBL of oil equivalent (BBOE) (Ko et al., 2017).

The Bakken Shale is one of the most prolific producing formations in the northern United States. It is an Upper Devonian-Lower Mississippian Shale play located in the Williston Basin of southern Saskatchewan, North Dakota, and eastern Montana (Fig. 1). Bakken Shale is greater than 100 ft thick in an extensive part of the Williston Basin (Peterson, 1996). Horsfield et al. (2008) reported a source rock maturity of 0.3–1.6 %

Ro. No uniform relationship exists between present-day thermal maturity and depth. However, the onset of intense hydrocarbon generation is usually 9000 ft and deeper (Webster, 1984). The organic matter is evenly distributed in the matrix (i.e., not concentrated in lenses or laminations) and averages about 11.3% (Webster, 1984). The US EIA (2014b) reported production of over 1 million barrels of oil per day from the Bakken. According to Hester and Schmoker (1985) another 7.4 billion BBL oil, 6.7 TCFG, and 527 MMBBL of natural gas liquids remain undiscovered, may be recovered from the Bakken Shale (Gaswirth et al., 2013).

3. Methodology and verification

The methodology of the porothermomechanical characterization for the shale plays under study and the procedure of a coupled porothermoelastic simulation in FLAC3D have been presented in the subsequent sections. The verification of each method has also been examined via key examples.

3.1. Porothermomechanical characterization methodology and verification

Amongst the physical, mechanical, PE, fluid, thermal, and porothermal parameters of a reservoir rock, some properties can be determined from the mineralogy of the rock (i.e., the percentage of each mineral in the reservoir rock), and the values of those properties for each mineral constituent. Some other properties are dependent on the former parameters and can be calculated afterwards. Thus, to determine all of the PTE properties, a probabilistic methodology is presented for estimating the required data for the reservoir rock as a whole based on its mineral composition, Monte Carlo stochastic sampling method, and the utilization of the averaging techniques.

In a polycrystalline rock with a mixture of small grains, different averaging methods can be used to estimate one average property from the mineral composition. With a simple laminated rock specimen, it is possible to explain the Voigt (V) and Reuss (R) averaging techniques (see Voigt. 1928; Reuss, 1929). Fig. 2 shows two laminated rocks, in which the direction of lamination to the direction of load application differs.

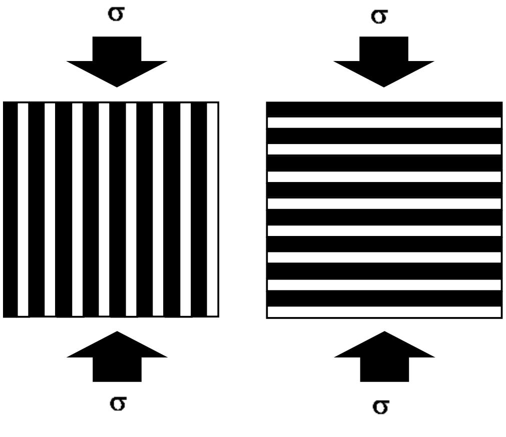

Figure 2. a) Voigt and b) Reuss averaging approaches

For the Voigt averaging technique, the direction of load application is assumed to be parallel with the lamination direction. For the case of Reuss averaging technique, on the other hand, the direction of load application is assumed to be perpendicular to the direction of lamination. According to the existing notion, the direction of load in polycrystalline isotropic rocks with respect to the spatial distribution of minerals is in between the two above-mentioned boundaries. Therefore, the average between the two above boundaries can be considered as a reasonable estimate for the property under study. This averaging method is called Voigt-Reuss-Hill averaging (VRH) which is the average of the two above boundaries (see Hill, 1952; Zuo et al., 1992). These averaging relations can be written as:

$$C_{Voigt} = \sum_{i=1}^{n} V_i C_i \tag{5a}$$

$$\frac{1}{C_{Reuss}} = \sum_{i=1}^{n} \frac{V_i}{C_i} \tag{5b}$$

$$C_{VRH} = \frac{C_{Voigt} + C_{Reuss}}{2} \tag{5c}$$

Using Eqs. (5a, 5b, 5c), one can obtain one average property for the reservoir rock by considering the percentage of each mineral and the associated property for each mineral. In the case of a wide range of variation in the percentage of mineral constituents, a wide range of variation for the reservoir rock property is also observed. Monte Carlo random sampling method was used to generate stochastic in-range mineral percentages, which together with the abovementioned averaging methods were used to obtain the distribution of different properties in the shale plays under study. The basic concept is to use randomness to solve this problem that is deterministic in principle. The concept implies that deterministic formulas exist for the resultant property (Eqs. 5), but using constitutive mineral volumetric proportions (V_i), a distribution was also obtained for the resultant property with its MV, skewness, and SD. This method is often used in many physical and mathematical problems. It is most useful when it is difficult to use other methods (e.g., McKean, 1967).

In this method, in order to have the range of variation for each property, a random number generator is used to produce mineral percentages within the predefined ranges, and then, normalizing them to a final sum of 100% considering the porosity of the rock. Then, for each set of mineral compositions, VRH averaging method was used and a final value was determined for one property. This property can be directly used as an input for the PTE simulation of the reservoir rock (e.g., grain moduli, rock porosity, Biot coefficient), or is used in a formulation which provides an input for the simulations. It is noteworthy that one relationship may have some input values, each having a statistical distribution, which result in a statistical distribution for the output as well (e.g. determination of Biot coefficient from drained bulk modulus and grain bulk modulus; or determination of Biot modulus from porosity, Biot coefficient, fluid bulk modulus, and grain bulk modulus; see Eqs. (7, 8)).

It is important to notice that the calculation of the skeleton properties is dependent on the anisotropic alignment of the mineral constituents. Therefore, a combination of Monte Carlo and VRH methods were used to obtain reasonable input data (MC-VRH). For the calculation of the properties of the pore-filling gas, the mineral constituent and alignment play no role and only Monte Carlo simulation was used for the characterizations (MC). The verification of the presented characterization method was performed for reservoir rock density in this section, and for other properties of the reservoir rock in the preceding sections (wherever reliable data have been reported in the literature).

To use MC-VRH method for the determination of a property, that property should first be available for each mineral constituent. The Most prominent constituents in the six shale plays are minerals such as quartz, plagioclase feldspar, calcite, and clay minerals (Smectite, Illite, Kaolinite, and Chlorite), total organic carbon (TOC), and porosity. The required properties are density, bulk and shear moduli, specific heat capacity, linear and volumetric thermal expansion coefficients, and thermal conductivity. These properties have been mentioned in Table 1. Mineral densities are from François (2008), Klein and Hurlbut (1985), and Okiongbo et al. (2005), bulk and shear moduli of minerals are from Martin (2017), Bass (1995), Lee (2004), Wang et al. (2017), Wang et al. (2001), Vanorio et al. (2003), Vernik (1993), Avseth et al. (2005), specific heat capacities are from Waples and Waples (2004), and Skauge et al. (1983), linear and volumetric thermal expansion coefficients of the selected minerals are from Dixon et al. (1993), Kingery et al. (1976), and McKinstry (1965). Thermal conductivity of minerals are from Cermak and Rybach (1982), Midttomme et al. (1998), Onishchenko et al. (2017).

Table 1. Mineral data used for MC-VRH methodology

Mineral	**Density**	**Bulk modulus**	**Shear modulus**	**Specific heat capacity**	**Linear expansion coefficient**	**Volumetric expansion coefficient**	**Thermal conduc-tivity**
units	Kg/m^3	GPa	GPa	J/kg˚K	×10^{-6} ˚C	×10^{-6} ˚C	W/m˚K
Quartz	2650	38.0	48.0	740	9.0	32.0	5.80
Plagioclase Feldspar	2680	75.0	29.0	730	10.0	30.0	1.53
Calcite	2712	75.0	26.0	815	20.0	60.1	3.40
Smectite	2394	10.0	6.5	818	13.0	39.0	1.80
Illite	2706	39.0	12.0	796	8.0	25.0	1.80
Kaolinite	2442	12.0	6.0	974	10.0	29.0	2.80
Chlorite	2681	81.0	27.0	600	10.4	31.2	3.10
TOC	1100	6.8	2.7	1500	0.01	0.01	0.10

The percentages of the above-mentioned minerals in each shale play according to the report presented by McKeon (2011) are shown in Table 2. The mineral percentage range mentioned in Table 2, together with their properties mentioned in Table 1, were used in MC-VRH to obtain the property ranges for each shale play.

Table 2. Real data for physical and Porothermoelastic properties of six different shale plays

Parameter	Unit	Marcellus	Woodford	Barnett	Haynesville	Eagle Ford	Bakken
Quartz	%	10.0-40.0	25-54	40-60	25-52	1.0-30.0	15.0-70.0
Plagioclase feldspar	%	0-10.0	7.0-13.0	2.0-5.0	8.0-17.0	0.0-17.0	1.0-3.0
Calcite	%	5.0-20.0	7.0-20.0	5.0-30.0	13.0-44.0	25-95	15-65
Smectite	%	<2	2.0-8.0	1.0-5.0	0.0	0.0-23.0	2.0-6.0
Illite	%	25.0-60.0	17.0-46.0	5.0-25.0	12.0-20.0	1.0-50.0	1.0-13.0
Kaolinite	%	<2	0.0	0.0	0.0	0.0-14.0	0.0-2.0
Chlorite	%	0.0-10.0	1.0	0.0	4.0-7.0	0.0-7.0	1.0-3.0
TOC	%	3.0-10.0	3.0-9.0	4.0-8.0	2.0-5.0	0.5-9.0	11.0-21.0
Porosity	%	3.0-8.0	1.0-8.0	1.5-6.0	8.0-15.0	3.0-15.0	2.0-12.0

To perform a precise analysis, apart from the shale skeleton, the properties of the gas present in pore spaces of these six shale plays were also reported. Methane, Ethane, Propane, Butane (C1-C4), Nitrogen (N_2), and Carbon dioxide (CO_2) are the main constituents of the gas in the host shale play. The molecular weights and their percentages in each shale play are reported in Table 3.

Table 3. Molecular weight and percentage of gas constituents in the six shale plays

Gas	Molecular weight	Critical temperature	Critical pressure	Marcellus	Woodford	Barnett	Haynesville	Eagle Ford	Bakken
unit	(gr/mol)	˚F	psi	(%)	(%)	(%)	(%)	(%)	(%)
C1	16.043	-117	673.3	85.20	95.7	86.75	95	74.6	47
C2	30.07	90	708	11.28	0.9	6.73	0.1	13.8	20
C3	44.097	206.1	617.4	2.88	0	1.98	0	5.4	14
C4	58.123	305.6	550.4	0.00	0	0.00	0	4.5	10.1
N2	28.013	-232.6	492.4	0.35	2.73	1.68	4.8	0.2	7.5
CO2	44.01	87.8	1071.6	0.30	0.67	2.88	0.1	1.5	1.4

The percentage of each gas, pseudo-critical pressure and temperature, and molecular weights are from Kort et al. (2016) and Brandt et al. (2015) for Bakken Shale, Hill et al. (2007) for Marcellus, Barnett, and Haynesville Shales, Harrington et al. (2015) for Eagle Ford Shale, Coates (2008) for Woodford Shale. The gas properties have been reported from research works performed by Bullin and Krouskop (2009), George and Bowles (2011), and Ezekwe (2011). Depending on the range of different gases in each shale play together with the gas properties, the MC method was applied for the determination of each property for each shale gas.

Depending on the depositional environment, depth, and location of the shale plays, the percentage of minerals may differ. Most of the major rock-forming minerals in the earth's crust, such as feldspar, quartz, and calcite, have very similar densities

(~2.5-2.7 g/cm^3). Kerogens have low densities in the range of 1.2-1.35 g/cm^3. Pyrite, on the other hand, has an exceptionally high density of ~5 g/cm^3. According to Taylor (2013), Lora et al. (2015), Boyce and Carr (2009), Sondergeld et al. (2010), the density of Marcellus Shale ranges from 2.27 to 2.66 g/cm^3. The density of Woodford Shale has been reported by Harris (2015), Bammidi (2011), and Ortega (2010) in the range of 2.2 to 2.7 gr/cm^3. The mean value of density for this shale has also been reported by Comer (2005) as 2.4 g/cm^3. The density of Barnett Shale has been reported in the range of 2.42-2.64 gr/cm^3 by Vermylen (2011), Kane (2006), Schmoker et al. (1996), Yu and Sepehrnoori (2013), and its mean value has been reported by Henry (1982) as 2.5 gr/cm^3. Jiang and Spike (2013), and Monfared (2015) reported the density of Haynesville Shale in the range of 2.2-2.7 gr/cm^3. Mokhtari et al. (2014) also reported the density of the Eagle Ford in the range of 2.33-2.49 g/cm^3. The Density of the Lower Bakken Shale ranges from 2.05 to 2.23 g/cm^3 with a median of 2.16 gr/cm^3, while the density of the Upper Bakken Shale ranges from 2.01 to 2.16 with a median of 2.09 g/cm^3 (Kohlruss and Stamatinos (2014)). Densities of the most common minerals in shale plays are reported in Table 1. The MV and SD of the densities of these shale plays can be determined using mineralogy, TOC, and porosity percentages were taken from Table 2 and constituent densities were taken from Table 1. The mineral percentages reported in Table 2 are inputs for the MC-VRH technique. The reported densities in the literature and the calculated density values via the MC-VRH technique are shown in Table 4.

Table 4. Density of the six shale plays, from literature and MC-VRH technique.

Property	Marcellus	Woodford	Barnett	Haynesville	Eagle Ford	Bakken
Reported density	2.27-2.66	2.2-2.7	2.42-2.64	2.2-2.7	2.33-2.49	2.01-2.23
Calculated density	2438±57	2472±57	2478±40	2366±55	2436±84	2297±97

As observed in Table 4, the predicted density values utilizing the MC-VRH technique are satisfactorily within the range reported in the literature. Therefore, the technique was used for the estimation of the most probable density range in the shale plays under study. It is worth mentioning that the obtained results are based on the percentage of each mineral mentioned in Table 2 and are subject to change depending on the volume percentages of different minerals in a specific shale.

Similar to the reported densities (see Table 4), the probabilistically generated data for different properties are reported as the MVs and their SDs. For the cases where laboratory data have been reported in the literature, a comparison is also made between the predicted and the reported property.

3.2. Numerical simulation methodology and verification

Core tripping with an analytical viewpoint is in the category of cylinder problem, which has been addressed based on the theory of poroelasticity and porothermoelasticity by several researchers (Abousleiman and Cui, (1998); Cheng (2016)). Core tripping is a process that includes pore pressure, temperature, and stress change, all of which happen during the core retrieval from the reservoir to the surface conditions. Appendix A shows the analytical solution of a PE core with constant and time-dependent boundary conditions (Abousleiman and Cui 1998). Appendix B also shows the PTE analytical solutions of a core problem with constant temperature and boundary conditions (Cheng 2016). There are some inevitable shortcomings associated with the available analytical solutions which are a) fixed values of the input parameters as fluid viscosity, rock permeability, specific heat, and thermal conductivity, b) availability of time-dependent boundary condition only for the PE case but not the PTE case, c) lack of an exact solution in time domain and the requirement of numerical approaches towards determination of their values in time domain, d) availability of the solutions only in the simplified two-dimensional case of plane-strain. Numerical solutions however, do not have the above limitations.

In our work, Fast Lagrangian Analysis of Continua in three dimensions (FLAC3D) developed by Itasca consulting engineers was used for the simulations. In the FLAC3D numerical code, a discretized form of Eqs. (4) using finite difference approximation has been derived which work in both explicit and implicit solution schemes. It is well-known that implicit finite difference method (FDM) in flow-only simulators such as Eclipse (Eclipse, 2017) are unconditionally stable, while there are boundary time steps in the explicit formulations, only below which converging results are expected. In fluid-mechanically coupled simulations, on the other hand, a limiting timestep exists for both of the explicit and implicit simulation schemes. Typically, the explicit method is used earlier in the run or in its perturbed stages, while the implicit method is preferred for the remainder of the simulation. Alternatively, the implicit method could be used with the explicit time step value for extra accuracy (FLAC3D manual, 2012). It is worth mentioning that flow time step in a PE simulation is dependent on the fluid characteristic time, which is the square of characteristic length over the fluid diffusivity. The thermal time step is also dependent on the thermal characteristic time, which is the square of characteristic length over the heat diffusivity. The concept of characteristic length is defined by the volume of diffusion over the diffusing surface area. The time step in a coupled porothermoelastic simulation is dependent not only on the above-mentioned factors (fluid and thermal diffusivities together with the characteristic length) but on the coupling terms of fluid and thermal diffusions as well.

In FLAC3D, brick-shaped zones described by eight nodes discretize the flow domain. The same discretization is used for mechanical and thermal calculations. Both pore pressure and temperature are assumed to be nodal variables. Internally, each zone is subdivided into tetrahedra, in which temperature and pore pressure are supposed to vary linearly. Starting from a mechanical equilibrium state, a coupled poromechanical static simulation in FLAC3D involves a series of steps. Each step constitutes one or more flow steps (i.e., flow loop) followed by enough mechanical steps (i.e., mechanical loop) to maintain quasi-static equilibrium. The increment of pore pressure arising from fluid flow is analyzed in the flow loop. The contribution related to volumetric strain is assessed in the mechanical loop as a zone value, which is further distributed to the nodes. The effect of temperature change on the volumetric change of the saturated matrix volume affects the coupling between thermal and flow-mechanical mode. For the application of thermal-fluid flow coupling, the FLAC3D grid requires configuration of fluid flow and thermal options.

Selection of wedge-and brick-shaped zones was performed for zoning of the core. Given the importance of grid aspect ratio (AR) in calculation accuracy in FLAC3D, a logical grid configuration was used with acceptable aspect ratios, small enough for capturing the high gradient of the fields and coarse enough for the computational effectiveness. Since the zone-wise sector length diminishes from the core rim to the core center, zone radial size diminishes in proportion to fulfill aspect ratio restrictions. Due to a high field gradient around the core surface, and small zone sizes required near the surface as well, a manually developed zone configuration was created using FISH programming in FLAC3D in order to consider aspect ratio limits, i.e., aspect ratio ≤4.00 around the center and aspect ratio ≥0.25 around the rim. Having applied this strategy, the high gradient of different fields was captured near the core surface and the high density of unnecessary zones was avoided in the core center (Fig. 2). Additionally, via FISH programming, we applied time-dependent boundary conditions, i.e., pore pressure, radial stress, temperature, and assignment of stress-, pore pressure-, and temperature-dependent properties.

In order to check the validity of the applied simulation method, it was necessary to model fundamental problems with existing analytical solutions. In this paper, two fundamental problems, i.e., PE cylinder with time-dependent stress and pore pressure boundary conditions (see Abousleiman and Cui 1998; Appendix A), and PTE cylinder problem with a constant temperature change on the core rim (see Cheng 2016; Appendix B) have been used for the simulations. The input parameters for the verification problems have been summarized in Table 5.

Table 5. Porothermoelastic data for the verification problems

Category	Parameter name	Symbol	Unit	Value
Physical	Porosity	ϕ	–	0.15
	Density	ρ	Kg/m^3	2450
Elastic	Young's Modulus	E	GPa	15.0
	Poisson's Ratio	ν	–	0.25
Fluid and Poroelastic	Undrained Poisson's Ratio	ν_u	–	0.31
	Biot Coefficient	α	–	0.57
	Biot Modulus	M	GPa	10.7
	Fluid viscosity	μ	Pa.s	0.001
	Absolute Permeability	k	m^2	10^{-18}
porother-moelastic	Specific Heat Capacity	C_p	Kg/J˚K	919
	Thermal Conductivity	k^T	W/m˚K	1.70
	Volumetric Expansion Coefficient	β_v	–	31.4×10^{-6}
	Undrained Thermal Expansion Coefficient	β_u	–	39.7×10^{-6}

Table 5 shows three PE constants of the rock. The input parameters have been used for the two aforementioned cylinder problems, the analytical solutions of which are available in the literature. The core radius was assumed as R=0.05 m. The assumed boundary conditions (BCs) for the two examples are as follows:

PE Cylinder with time-dependent BCs

$$\begin{cases} p(t) = 0.15t \\ \sigma_r(t) = 0.15t \end{cases} ; \quad \begin{matrix} t = 0 - 100\ s \\ r = R \end{matrix}$$

PTE Cylinder with a constant BC

$$\Delta T = 20℃\,; \quad \begin{matrix} t = 0 - 100\ s \\ r = R \end{matrix}$$

The results of the simulations are shown in Fig. 3, which shows that the pore pressure and stress fields (radial and tangential) match the analytical solutions well.

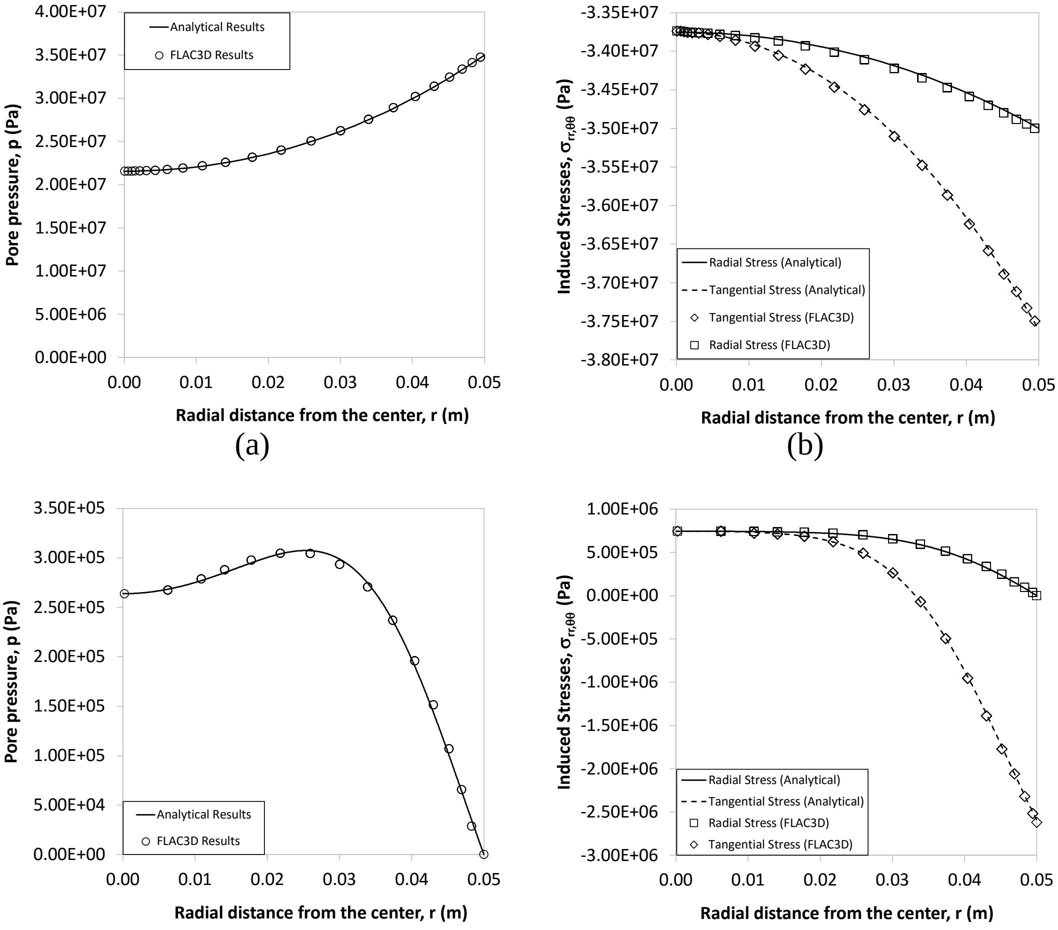

(a) (b)

(c) (d)

Figure 3. Verification of the induced pore pressure and stresses (radial and tangential) for two different problems; a, b) poroelastic cylinder problem with a time-variable boundary condition; c, d) porothermoelastic cylinder problem with temperature boundary condition (R=0.05 m)

3.3. Trip velocity estimation method

The initial assumptions for simulation of core retrieval are a) negligible effect of coring operation (i.e., core-rock bit collision, core attachment to the bottom of the wellbore, permeability change of the core rim), b) balanced drilling mode, c) core oriented normal to the bedding plane and with a diameter of 0.1 m, d) plain strain condition with no effect of plasticity and convection in the thermal-fluid logic.

Trip velocity determination is highly dependent on the tensile strength of the reservoir rock. It is obvious that with higher tensile strength of the core, the tripping velocity can consequently be higher as well. It is worth mentioning that a factor of safety of 1.2 was considered for the tensile strength. The highest stress state which may cause tensile failure is the tangential stress which peaks at the core rim (Taghichian et al. 2018). Therefore, the tangential stress on the core rim obtained from the numerical simulations was compared with the tensile strength of the core divided by the safety factor. The trip velocity which results in this equality is taken as the optimized trip velocity, which is high enough to take the core to the surface in the shortest time and is slow enough to prevent damages.

Because of the large variations in the magnitudes of each parameter, to optimize the trip velocities, it was first required to determine which combination of parameters for a shale play results in the most conservative, the mean, and the least conservative cases. Therefore, a magnitude range for each parameter was required. Depending on the direct/inverse relationship between the input variable and the induced stresses (see Taghichian et al. 2018), three sets of simulations were performed for the the most conservative, the mean, and the least conservative magnitudes.

This work has been executed with the following objectives for all the above-mentioned shale plays: a) Perform geomechanical characterization resulting in the MV and SD for each property; b) perform coupled PTE simulation of the core tripping job in the six shale plays using the least, mean, and most conservative scenarios; c) find core-tripping velocity range for each shale play utilizing the presented scenarios in a PTE simulation scheme.

4. Probabilistic PTE characterization of the reservoir rocks

The probabilistic estimation of the PTE properties for the reservoir rock and the pore-filling gas was respectively performed using MC-VRH and MC simulation methods.

4.1. Gas properties

The gas constituents for mentioned shale reservoirs are reported in Table 3. Deterministic methods for calculation of gas properties presented by Kareem et al. (2014) for specific heat capacity, Lee et al. (1966) for gas viscosity, Jarrahian and Heidarian (2014) for gas thermal conductivity, and Ezekwe (2011) for compressibility and gas bulk modulus were used in the probabilistic MC method. The outcome was to determine the pseudo-critical pressures and temperatures (p_{pc}, T_{pc}) and then the reduced pressures and temperatures (p_{pr}, T_{pr}). Thereafter, the ideal and residual specific heats were calculated, using which the actual specific heats were determined. The results of these simulations are shown in Table 6; rows 3-8. The initial temperatures and pore pressures of these shale reservoirs were used for the determination of gas properties (See Table 3; Appendix C).

It is observable from Table 6; row 6 that the mean values for the bulk modulus of pure gas in the pore spaces of the shale plays under study lie between 0.04 to 0.29 GPa for the valid range of temperature and in-situ pore pressure. The bulk modulus of water is 2.4 GPa. The bulk moduli of oil and condensates lie in between those of gas and water. The range of bulk modulus for the fluid content in the shale plays is important in the determination of Biot modulus.

Table 6. Porothermoelastic characterization of six major unconventional shale plays in the US.

No.	Property	Unit	Marcellus	Woodford	Barnett	Haynesville	Eagle Ford	Bakken
1a	Calculated density	kg/m^3	2438±57	2472±57	2478±40	2366±55	2436±84	2297±97
2b	Reported density	gr/cm^3	2.27-2.66	2.2-2.7	2.42-2.64	2.2-2.7	2.33-2.49	2.01-2.23
3a	Gas Specific heat capacity	J/Kg/K	5023±230	4640+138	4662±109	4474±22.8	5112±455	4799±229
4a	Gas Thermal conductivity	W/m ˚K	0.059±0.006	0.076+0.009	0.062±0.004	0.115±0.006	0.076±0.013	0.070±0.004
5a	Gas compressibility	$\times 10^{-5}$ psi^{-1}	18.48±6.84	10.85+4.68	16.67±4.06	2.52±0.64	8.95±5.46	8.890±1.60
6a	Gas bulk modulus	$\times 10^{-2}$ GPa	4.25±1.52	7.55±3.08	4.38±1.03	29.34±8.10	10.76±6.58	8.00±1.45
7a	Gas density	gr/cm^3	0.192±0.037	0.209±0.036	0.190±0.025	0.233±0.011	0.336±0.067	0.322±0.028
8a	Gas viscosity	cP	0.023±0.003	0.026±0.004	0.023±0.002	0.031±0.001	0.044±0.013	0.039±0.005
9b	Reservoir thickness	m	0-290	38-274	30-152	30-107	8-152	15-76
10b	True Vertical Depth	m	1372-2591	1829-4267	1646-2896	3200-4267	1524-3962	2438-3353
11b	Vertical stress	MPa	59	57.5	65	85	80	54
12b	Max. horizontal stress	MPa	49.8	60	64-85	83	85	42
13b	Minimum horizontal stress	MPa	34.2	52	44-47	80	70	29
14b	Initial pore pressure	MPa	30	27.6	30	70	60	28
15b	Vertical stress gradient	KPa/m	23.98	23.98	24.20	23.07	23.98	22.85

No.	Property	Unit	Marcellus	Woodford	Barnett	Haynesville	Eagle Ford	Bakken
16b	Max. horizontal stress gradient	KPa/m	20.13	20.36-25.11	23.98-31.9	22.62	25.34	17.64
17b	Min. horizontal stress gradient	KPa/m	13.80	17.42-21.72	16.51-17.64	21.72	20.81	12.22
18b	pore pressure gradient	KPa/m	9.05-18.55	10.18-15.38	11.31-21.04	19.23	9.05-19.23	11.31-13.57
19a	Initial Pore pressure	MPa	24.65±5.90	38.94±10.15	26.71±4.25	75.17±6.51	38.79±12.98	36.03±3.79
20b	Initial Temperature	˚C	38-66	66-107	66-88	138-193	66-177	88-116
21a	Grain Bulk Modulus	GPa	37.5±2.27	36.5±1.72	36.5±2.19	47.0±2.25	41.4±4.84	34.8±3.28
22a	Grain Shear Modulus	GPa	18.1±1.83	21.1±1.64	24.7±1.40	25.5±1.34	18.0±2.02	19.8±2.24
23b	Dry Young's Modulus	GPa	8.31-20.8	16.6-33.3	24.9-41.6	8.31-12.5	4.16-16.6	8.31-24.9
24b	Dry Poisson's Ratio	-	0.19-0.23	0.15-0.25	0.13-0.25	0.23-0.27	0.20-0.27	0.2-0.25
25a	Dry Bulk Modulus	GPa	8.38±2.10	14.0±3.04	18.1±3.34	6.95±0.87	6.57±2.33	10.09±2.96
26a	Dry Shear Modulus	GPa	6.01±1.49	10.4±2.03	13.98±2.07	4.16±0.49	4.21±1.46	6.78±1.96
27a	Reported Biot Coef.	-	0.6	0.74-0.81	1.0	0.97	0.95	0.45-0.53
28b	Calculated Biot Coef.	-	0.78±0.06	0.62±0.09	0.5±0.1	0.85±0.02	0.84±0.06	0.71±0.09
29a	Calculated Biot Mod.	GPa	8.87±4.53	12.64±7.16	14.31±7.41	5.2±2.71	8.33±4.70	9.01±5.13
30a	Skempton coefficient, B	-	0.48±0.17	0.39±0.18	0.32±0.15	0.39±0.14	0.53±0.19	0.41±0.19
31a	Undrained Bulk modulus, K_u	GPa	13.68±2.93	18.80±3.48	21.77±2.96	10.67±1.93	12.40±3.79	14.64±3.45
32a	Poisson's ratio diff. (ν_u-ν)	-	0.10±0.04	0.064±0.038	0.044±0.028	0.074±0.028	0.109±0.048	0.073±0.041

No.	Property	Unit	Marcellus	Woodford	Barnett	Haynesville	Eagle Ford	Bakken
33b	Porosity	%	3.0-8.0	1.0-8.0	1.5-6.0	8.0-15.0	3.0-15.0	2.0-12.0
34a	Specific heat capacity	J/Kg/K	927±40	893±43	876±26	1004±45	960±64	988±69
35a	Linear expansion coefficient	$\times 10^{-6}$ °C	9.81±0.42	10.06±0.35	10.57±0.60	11.39±0.60	13.34±1.19	12.84±1.13
36a	Volumetric expansion coefficient	$\times 10^{-6}$ °C	31.34±1.27	32.61±1.07	35.07±1.74	36.65±1.66	41.10±3.44	41.56±2.97
37b	Reported Thermal conductivity	W/m °K	1.70	1.77	1.78	1.72	1.5	1.74
38a	Estimated Thermal conductivity	W/m °K	1.71±0.17	1.99±0.17	2.37±0.12	1.94±0.12	1.75±0.19	1.92±0.21
39b	Permeability range	μd	0.2-2.0	0.05-0.40	0.05-0.40	0.001-0.005	400-1200	20-500
40b	Effective stress coefficient, χ	-	0.15	0.65	0.68	0.40	0.82	0.46
41b	Permeability at lower stress, k_{max}	nd	56	250	159	40	53	724
42b	Permeability at higher stress, k_{min}	nd	20	15	65	3	10	326
43b	Lowest measurement stress, σ_{emin}	psi	1865	1010	1330	4877	1580	851
44b	Highest measurement stress, σ_{emax}	psi	6534	3006	5283	10724	6400	2335
45b	Coefficient a, Eq. (9)	-	5.223	19.860	2.045	0.277	68.946	0.472
46b	Coefficient b, Eq. (9)	-	0.186	0.057	0.472	3.282	0.009	2.116
47b	Coefficient c, Eq. (9)	-	0.105	-0.712	-0.277	-3.050	0.333	-1.262
48b	Tensile strength	MPa	4.1	6.5	6.6	4.6	4.4	12.5

4.2. Reservoir in-situ properties

In order to perform precise and acceptable porothermoelastic simulations, apart from the required porothermoelastic parameters of the reservoir rock, in-situ variables of the shale plays are of paramount importance as well. The in-situ properties of a reservoir include reservoir thickness, lateral extent, true vertical depth (TVD), stresses, initial pressure, and temperature. Reservoir thickness and its lateral extent provide an idea about the potential hydrocarbon content. They are also important in determining the effective fracture height during hydraulic fracturing jobs. TVD provides information about the type of hydrocarbon, i.e., rocks at lower depths may be immature or oil prone, while those at higher depths may be gas prone due to overcooking. TVD also provides an idea of the expected stresses, pore pressure, and temperatures if the general stress, pressure, and temperature gradients are known. Having an estimate of the reservoir depth is also important for the optimization of the core tripping velocity (See Taghichian et al., 2018). Reservoir depth plays a decisive role with respect to core damage due to its effect on diffusion time and thermal contraction while tripping. The above-mentioned in-situ properties are reported in Table 6; rows 9-20.

In-situ properties of the Marcellus Shale are reported from Han and Yin (2018), EIA (2017a), Zagorski et al. (2011), and Zagorski (2016); Woodford Shale from Hair (2014), Abousleiman et al. (2014), McKeon (2011), McCullough (2014), Wickstrom (2008), and Ghosh (2017); Barnett Shale from Sone and Zoback (2014), Bammidi (2011), McKeon (2011), and World Oil (2015); Haynesville from LeCompte et al. (2009), and Chun (2013); Debrick (2017), EIA (2017b), Eagle Ford from Suppachoknirun and Tutuncu (2017), Stidham (2011), EIA (2014a), and McKeon (2011); and Bakken from Havens (2012), EIA (2014b), Redlinger (2015). We obtained the initial pore pressure via pore pressure gradient and TVD range mentioned in Table 6; row 19 as inputs to MC. Comparing the values expressed in Table 6; rows 14b and 19a, one can see that the reported values in the literature are only single values, while the values obtained in the MC simulations provide give range of pore pressure variation for the shale plays.

4.3. Poroelastic properties

To estimate the mechanical (grain bulk- and shear moduli) and PE properties of the shale plays, the MC-VRH technique was used. Thereafter, the range of dry Young's modulus and dry Poisson's ratio (see Table 6; rows 23, 24) were used for determining the drained bulk modulus. It is noteworthy that using MC method, K_d distribution can be determined using Eq. (6). The MC-VRH method was then used with the distribution of K_g in order to determine Biot coefficient using Eq. (7). Finally, the distribution of porosity, Biot coefficient, fluid bulk modulus, and grain modulus were used for Biot modulus distribution.

$$K_d = \frac{E_d}{3(1-2\nu_d)} \tag{6}$$

$$\alpha = 1.0 - \frac{K_d}{K_g} \tag{7}$$

$$\frac{1}{M} = \frac{\phi}{K_f} + \frac{\alpha - \phi}{K_g} \tag{8}$$

The Biot coefficient of Marcellus Shale was assumed by Kowan and Ong (2016) as 0.6. For Woodford Shale it was reported by Abousleiman et al. (2008) as 0.74-0.81 and between 0.75-0.97 by Ghosh et al. (2019). For Barnett Shale it was assumed by Rutqvist et al. (2013) and Sone and Zoback (2014) as 1.0. For Haynesville Shale it was assumed by Chun (2013) as 0.97. For Eagle Ford Shale it was assumed by Suppachoknirun and Tutuncu (2017) as 0.95, and for Bakken Shale it was reported by Havens (2012) in the range of 0.45-0.53.

Upon comparing the reported and the estimated Biot coefficients, one can see that the reported values are reasonably well in or close to the range of (MV$\pm$3 SD), within which 99.7% of the total dataset volume. The reported Biot coefficient of Barnett Shale, however shows the highest difference, which is 20% out of the presented range. It is implied from Rutqvist et al. (2013) that the considered Biot coefficient is an assumed value rather than a laboratory measured value. Sone and Zoback (2014) mentioned that the value of Biot coefficient in theBarnett Shale is an assumed value.

According to Eq. (7), Biot coefficient is influenced by grain moduli and dry bulk moduli. Since, in this study, we have used static bulk moduli in Eq. (7), we should also use static dry moduli in the MC-VRH method for Biot modulus estimation (Eq. (8)). However, for most cases, the available moduli of the mentioned shale plays were derived from well logs and may be considered dynamic moduli. There are several relationships between static and dynamic moduli developed by researchers (e.g., Willis, 2013). We have used an equation developed by Hall (2010) as $E_s = 0.6029E_d$ in which E_s and E_d are the static and dynamic moduli of the rock respectively. For Poisson's ratio, no well-defined dynamic to static relationship exists. Barree et al. (2009) concluded that the dynamic Poisson’s ratio can suitably approximate the static value irrespective of the stress state. We have reported the estimated range of elastic and PE properties in Table 6; rows 21-33.

Considering Eq. (8), one can realize that fluid bulk modulus highly influences the Biot modulus. According to Loucks et al. (2012) and William (2012), gas is not the only phase that exists in all pore spaces of shales, i.e., water, oil, gas, and condensates can coexist in the pores. This phenomenon highly influences the compressibility of the pore fluid (reverse of fluid bulk modulus). Dadashpour et al. (2009) stated that the fluid bulk moduli in shales are in the range of 0.1-1 GPa which can be considered a combination of bulk moduli of water, oil, and shale gas (see Table 6; rows 3-8). Therefore, using Eq. (8), the range of Biot coefficient obtained from Eq. (7), the range of porosity for each shale play, and the range of fluid bulk moduli from Dadashpour et al. (2009), we can obtain the range of Biot modulus for each shale play.

As it shown in Table 6; rows 21-33, all the PE parameters were implemented inside and derived from determination of grain moduli using the MC-VRH technique. It is obvious that the presented results are highly dependent on the percentage of each mineral constituent, which is subject to lateral and vertical changes in addition to its association with the reservoir type (Appendix D-I). As seen in Table 6; rows 30-32, the highest difference between drained and undrained Poisson's ratio exists in the Marcellus and Eagle Ford Shales and the least in the Woodford Shale.

Numerous researchers have shown that shale permeability changes with confining pressure. However, in order to have a robust equation for relating the permeability and confining pressure, an effective stress coefficient (χ) is used. The effective stress coefficient is used for the determination of the effective confining stress as $P - \chi p$, in which P is the confining stress and p is pore pressure. The effective stress coefficients (see Table 6; row 40b) and the permeability values $k(P - \chi p)$ have been reported by

Heller et al. (2014) for Eagle Ford and Marcellus Shale, Cho et al. (2013) for Bakken Shale, Vermylen (2011) for Barnett Shale, Bustin et al. (2008) for Woodford Shale, and Hosseini Boosari et al. (2016), LeCompte et al. (2009) for Haynesville Shale. All the $k(P-\chi p)$ data follow an exponentially decreasing trend shown by Eq. (9) developed by the authors (see Taghichian et al. 2018). Therefore, the following intrinsic function of permeability can be used for the six shales.

$$k(\sigma_e)=\begin{cases} k_{max} & \sigma_e \le \sigma_{emin} \\ k_{min}ab^{(\sigma_e/\sigma_{emax})}(\sigma_e/\sigma_{emax})^c & \sigma_{emin}\le\sigma_e\le\sigma_{emax} \\ k_{min} & \sigma_e \ge \sigma_{emax} \end{cases} \tag{9}$$

where k_{min} is the permeability at the highest confinement tested, $\sigma_{emax}=P_{max}-\chi p_{max}$ is the highest effective confinement at which the permeability was determined, k is the permeability to be determined under the specific effective stress $\sigma_e=P-\chi p$, and a, b, c are the coefficients of the presented relationship (see Table 6; rows 41-47).

4.4. Thermoelastic properties

The thermoelastic (TE) property values, together with their range of variation, were also determined using MC-VRH technique and are reported in Table 6-rows 34-38 (See also Appendix D-I). The reported thermal conductivities of the shale plays have also been reported from Perry et al. (2014). Comparing the estimated MC-VRH values and the reported values of thermal conductivity, one can see that all the reported data are well in the range of (MV±3 SD), within which 99.7% of the data should be placed, except for the Barnett shale, which comes with 13% of error outside of the range.

5. Coupled PTE and TE simulations

Based on the reported MVs (see Table 6), two series of simulations, one with the PTE approach and the other with the thermoelastic (TE) approach, were performed. According to Taghichian et al. (2018), the behavior of PE and PTE induced stresses in the core was significantly different. The noticeable difference was attributed to the effect of temperature, which existed in the PTE but not in the PE approach. In addition, the induced stresses in the PTE scheme was more critical compared to those in the PE approach. The results of the simulations are presented and compared herein for five different simulation times in the range of $t_n = 0.2-1.0$, where t_n is the normalized time and is defined as the simulation time over the travel time from reservoir depth to the surface (Fig. 4). As pore pressure exists for the case of PTE scenario, the effective stresses were calculated based on the values of the Biot coefficient, the pore pressure, and the total stresses.

As it is evident in Fig. 4, effective tangential stresses in the core have been depicted that are the most critical induced stresses which may cause failure. Although the global trend of the induced stresses in the two approaches (PTE and TE) is the same, a significant difference exists between the stress values for $t_n < 1$. The PTE stress curves have less compressive states and are more close to each other compared to those from the TE approach. The reason for this observation is that stresses in the TE core are directly controlled by temperature and confining stresses. In case of PTE core, on the other hand, the stresses are controlled by temperature, confining stress, and pore pressure as well. Therefore, the present pore pressure in the core highly reduces the difference between the effective stresses in the PTE scheme.

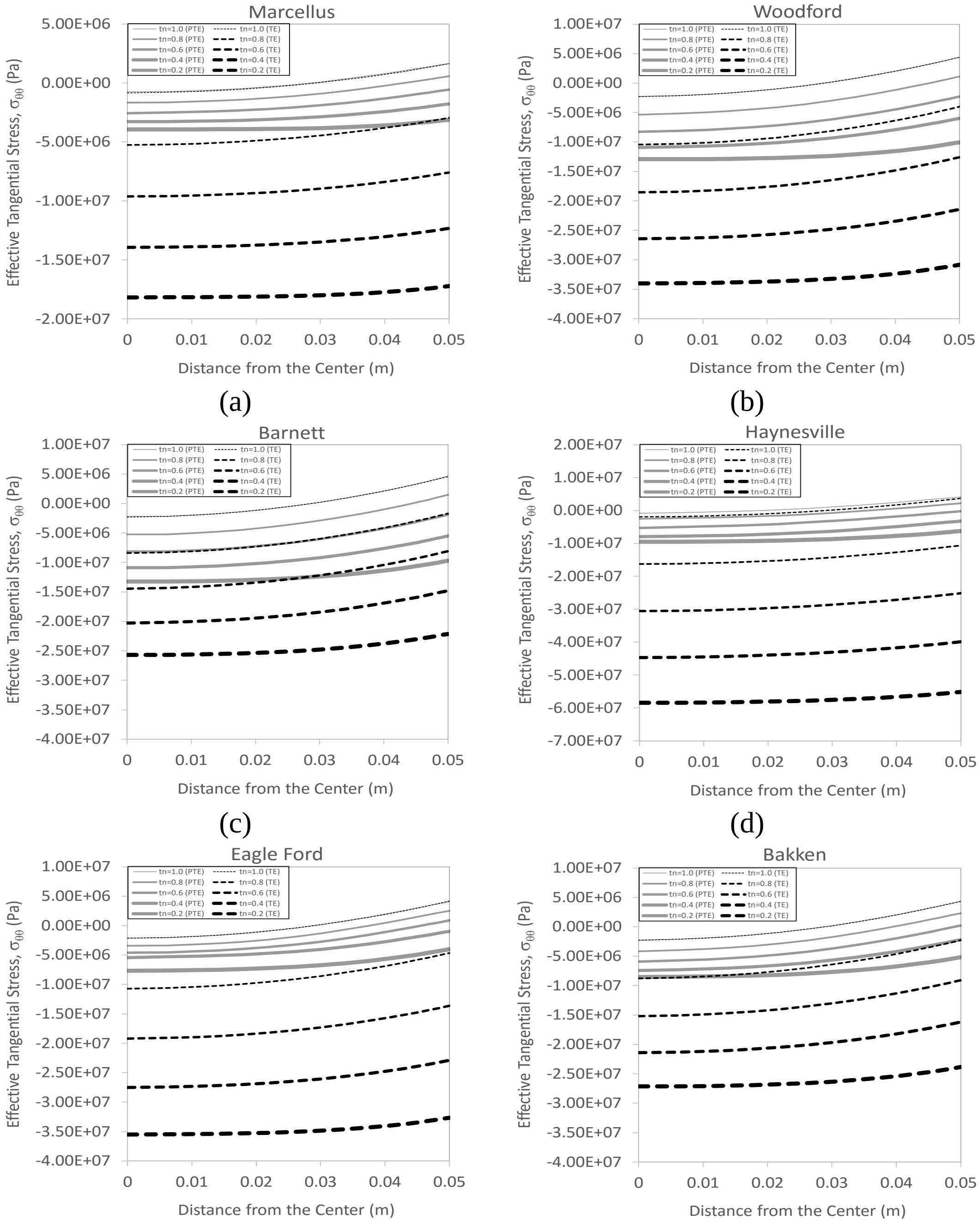

(a) (b)

(c) (d)

(e) (f)

Figure 4. Evolution of effective tangential stress during tripping in two different schemes, i.e., porothermoelastic (PTE) and thermoelastic (TE) in a) Marcellus, b) Woodford, c) Barnett, d) Haynesville, e) Eagle Ford, and f) Bakken Shales.

It is also observed that the effective tangential stresses at $t_n = 1.0$ nearly coincide with each other for the two approaches of PTE and TE except for Haynesville shale. The main reason of this coincidence is that there are two controlling mechanisms in reducing the pore pressure in the core. The first mechanism is the reduction of pore pressure because of fluid diffusion as a result of lower pore pressure on the core rim. The second mechanism is the instant reduction of pore pressure as a result of confining stress decrease and Skempton's effect which was explained by Taghichian et al. (2018). Therefore, since confining stresses no longer exist on the core surface, pore pressure vanishes because of diffusion and Skempton's effect. Only the thermal stresses still exist in the core, which have also been simulated in the TE scheme. Under these conditions, the results from PTE and TE approaches are comparable. For the case of Haynesville shale however, a lower permeability level exists with respect to the other shales, thereby raising the required fluid diffusion time. This behavior proves that TE and PTE simulation results are not always the same at surface conditions ($t_n = 1.0$). Therefore, to obtain the tripping velocity range, the PTE simulation scheme was used for investigating the mechanism of effective stress evolution during tripping.

To obtain a reasonable range of tripping velocity for the six aforementioned shale plays, the most conservative, the mean, and the least conservative simulations have been performed based on the ranges of data reported in Table 6. Taghichian et al. (2018) performed a comprehensive sensitivity analysis in which the PTE properties were changed by some percentage (decreasing/increasing) and their influence on the induced stresses were investigated. The resultant relationships have been mentioned in Table 7. Therefore, using the relationship between the input variables and the resultant stresses, one can easily choose between boundary values to obtain the most conservative, the mean, or the least conservative scenario.

Table 7. Direct and reverse relationship between input parameters and the induced stresses

Parameter	Simulation method	Relationship
Biot's coefficient α	Poroelastic	direct
Rock Young's Modulus, E		reverse
Fluid Mobility, κ		reverse
Poisson's Ratio, ν		direct
Tripping velocity, V		direct
Undrained Poisson's Ratio, ν_u		reverse
Biot's coefficient α	Porothermoelastic	-
Rock Young's Modulus, E		direct
Fluid Mobility, κ		-
Poisson's Ratio, ν		direct
Tripping velocity, V		direct

Undrained Poisson's Ratio, ν_u		direct
Linear Expansion Coefficient, α_L		direct
Rock Density, ρ		direct
Specific Heat Capacity, C_p		direct
Temperature, T		direct
Undrained Expansion Coefficient, β		direct
Thermal conductivity of Rock, λ		reverse

The effective induced stresses versus the tripping velocities of the core using the most, the mean, and the least conservative input values are shown in Fig. 5. As demonstrated in Fig. 5, the increase of the induced stresses in the core versus the applied trip velocity highly varies between different shale plays. Fig. 5 shows that there is a wide range of stress variation due to different values of trip velocity. The values of stresses are in the range of 1.0-18.0 MPa, 1.8-8.6 MPa, and 0.5-5.5 MPa for the most, the mean, and the least conservative scenarios. It is also worth mentioning that in the mean scenario, the velocity-tangential stress curves follow a certain trend for all the simulated shale plays except for the Marcellus Shale.

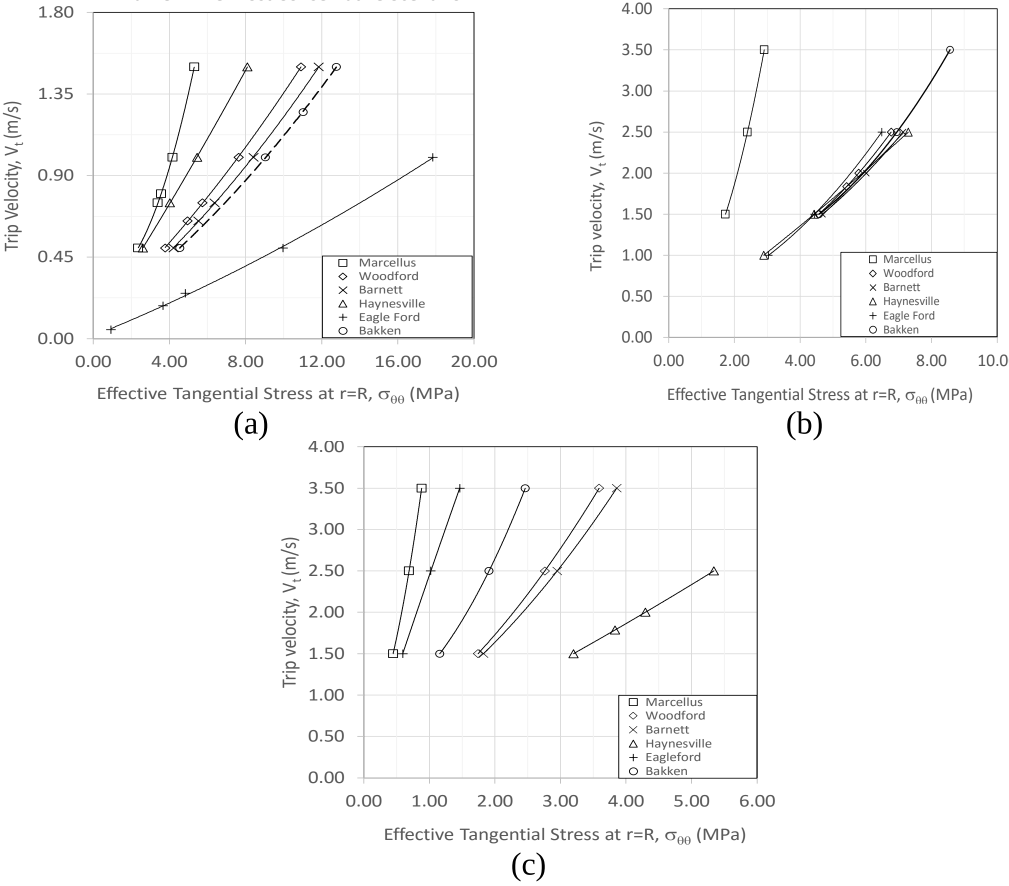

(a) (b)

(c)

Figure 5. Induced stresses as a result of trip velocity change for the a) most, b) mean, and c) least conservative scenarios in different shales.

For the given mineral compositions in the six shale plays (Table 2), the values of tensile strengths (Table 6; row 48b), and the assumed factor of safety (≈1.2), the range of safe trip velocities were estimated and reported in Table 8. As observed in Table 8, for the most conservative scenario, Marcellus, Woodford, Barnett, and Haynesville shales have trip velocities in the order of 0.64-0.75 m/s, but Eagle Ford and Bakken have trip velocities of 0.18 and 1.17 m/s respectively. The small trip velocity of the Eagle Ford is because of the combined effect of high linear thermal expansion coefficient, low thermal conductivity, high reservoir temperature level, and low tensile strength. The high trip velocity of Bakken shale, on the other hand, comes from its high tensile strength. There are some scenarios in which the tripping velocities could not be estimated because the induced stresses were much lower than the tensile strength of the rock, even for the tripping velocities as high as 3.5 m/s. Therefore, the tripping job for these scenarios were assumed as safe for a normal tripping velocity. In the mean scenario, Marcellus shale has lower stress levels compared to the other shales, which comes from the combining effect of low linear thermal expansion coefficient and low reservoir temperature level. In the least conservative scenario, Haynesville shale has the highest stress levels, which comes from very high reservoir temperature levels. It is quite evident that the most critical stress levels in each of the three scenarios occur because of thermal effects. As mentioned previously, the main reason for this phenomenon is the rapid fluid diffusion in the core due to Skempton's effect and the decreasing pore pressure boundary condition.

Table 8. The optimized trip velocity for the most, the mean, and the least conservative scenarios of the shale play

Case condition	Unit	Marcellus	Woodford	Barnett	Haynesville	Eagle Ford	Bakken
The most conservative scenario	m/s	0.75	0.71	0.64	0.71	0.18	1.17
The mean scenario	m/s	-	1.84	1.79	1.30	1.21	-
The least conservative scenario	m/s	-	-	-	1.79	-	-

The average diffusion times for fluid and thermal phases have been calculated and their ratios have been reported in Table 9. As observed in Table 9, the ratio of thermal diffusion time over fluid diffusion times is always larger than unity and can vary from 7.5 to 290. As mentioned in the previous sections, fluid and thermal characteristic times are characteristic length over the fluid and thermal diffusivities, and have been calculated independent of the initial conditions. In Table 9, despite the fact that fluid characteristic time in Haynesville Shale is smaller than that in Eagle Ford Shale, its remaining pore pressure is larger than that in Eagle Ford, and results in larger PTE (compared to TE stresses) at surface conditions (see Fig. 4). The possible reason for this observation is the high value of remaining pore pressure in Haynesville Shale compared to those in the other shales.

Table 9. The comparison of fluid and thermal diffusion processes

Variable	**Symbol**	**Unit**	**Marcellus**	**Woodford**	**Barnett**	**Haynesville**	**Eagle Ford**	**Bakken**
Confining stress	P	MPa	34.20	52.00	44.00	80.00	70.00	29.00
Skempton coefficient	B	-	0.48	0.39	0.32	0.39	0.53	0.41
Pore pressure change	Δp	MPa	16.42	20.28	14.08	31.20	37.10	11.89
Initial pore pressure	p_i	MPa	30.00	27.60	30.00	70.00	60.00	28.00
remained pore pressure	p_r	MPa	13.58	7.32	15.92	38.80	22.90	16.11
Min Permeability	k_{min}	nd	20.00	15.00	65.00	3.00	10.00	326.00
Max Permeability	k_{max}	nd	56.00	250.00	159.00	40.00	53.00	724.00
Average Permeability	k_{avg}	nd	38.00	132.50	112.00	21.50	31.50	525.00
fluid characteristic time	t_c^f	s	154.92	39.30	42.93	411.41	526.12	11.36
Thermal characteristic time	t_c^h	s	3311.10	3186.19	3056.54	3437.88	3952.67	3294.83
Ratio of characteristic times	t_c^f/t_c^h	-	21.37	81.07	71.19	8.36	7.51	289.91

6. Conclusion

This work proposes an optimization method presenting a safe core tripping velocity range. The presented method was consisted of a coupled PTE simulation with time-varying thermal, pore pressure, and stress boundary conditions, which were performed based on a probabilistic PTE characterization founded on the available data from literature. This characterization resulted in pinpointing mean value and the standard deviation for the required parameters in the PTE numerical simulations. The presented characterization methodology provides several practical benefits. First, it presents a methodology of combining field data with the mineral constituents of the reservoir rock and different mineral properties to estimate, verify, and present probabilistically determined meaningful/in-range data. The provided data can be used for later referrals when performing laboratory- or industry-related work. In other words, it provides researchers reasonable data ranges of the reservoir rocks, which are more accurate assumed arbitrary values with no experimental or field background. Second, it provides a comparison of the properties for six US shale plays, i.e., Marcellus, Woodford, Barnett, Haynesville, Eagle Ford, and Bakken, which can also be reobtained based on the specific mineralogy ranges of the different shales. Third, it creates the opportunity of performing PTE and TE simulations based on comparable/reasonable input parameters and feasibility study of less intense/fast TE simulations as a substitute for the complex, time-consuming, and expensive PTE simulations. The simulations themselves also resulted in a number of fundamental key points regarding the core tripping jobs in unconventional shales. First, TE simulations result in similar results for the case of $t_n = 1.0$ (i.e. when the core reaches to the surface). However, care should be taken for this analogy because for some cases, the remaining pore pressure inside the core is large and requires more time to dissipate. In such cases, one table similar to Table 9 should be produced for the rock core and the results should be analyzed accordingly. Second, the gradual changes of the effective stresses in the two simulation approaches of TE and PTE are not comparable and TE simulations cannot be used as a substitute for PTE simulations. Third, the estimated trip velocities based on the assumption of the most, the mean, and the least conservative scenarios can result in completely different judgments of safe tripping velocities. Therefore, it is recommended that the data which is to be used for the simulations be examined, analyzed, and validated. Fourth, in case of analyzing similar shale plays as the ones presented in this study, in combination with the knowledge of the mineral contents for the shale under study, a MC and MC-VRH analysis can be used. Then, a comparison can be made between the properties of the shale under study and those of the most, the mean, and the least conservative scenarios. Finally, a reasonable core trip velocity can be estimated for the shale under study, considering the initial conditions of the reservoir and the required factor of safety.

Acknowledgement

Sincere thanks to the University of Oklahoma (Norman, USA) for supporting this research

References

[1] Abousleiman, Y.N., Tran, M.H., and Hoang, S., 2008. Laboratory Characterization of Anisotropy and Fluid Effects on Shale Mechanical Properties Using Inclined Direct Shear Testing Device IDSTD. American Rock Mechanics Association 08-256.

[2] Abousleiman, Y.N., Hoang, S.K., and Liu, C., 2014. Anisotropic porothermoelastic solution and hydro-thermal effects on fracture width in

hydraulic fracturing. International Journal for Numerical and Analytical Methods in geomechanics, 38, p. 493-517. Doi: 10.1002/nag.2216

[3] Abousleiman, Y., and L. Cui. 1998. Poroelastic solutions in transversely isotropic media for wellbore and cylinder. Int. J. Solids Struct. 35 (34–35): 4905–4927. https://doi.org/10.1016/S0020-7683(98)00101-2.

[4] Amsden, T.W., 1975. Hunton Group (Late Ordovician, Silurian, and Early Devonian) in the Anadarko basin of Oklahoma. Oklahoma Geological Survey Bulletin, 121, p. 214.

[5] Avseth, P., Mukerji, T., and Mavko, G., 2005. Quantitative seismic interpretation: Applying rock physics tools to reduce interpretation risk. Cambridge university press. Online ISBN: 9780511600074 https://doi.org/10.1017/CBO9780511600074.

[6] Auman, J.B., 1986. A laboratory evaluation of core preservation materials. Richardson, TX: SPE.

[7] Bammidi V.S., 2011. Unconventional Oil & Gas Resource Evaluation of the Woodford Shale in New Mexico. Master's thesis, New Mexico Institute of Mining and Technology (NMT).

[8] Bass, J.D., 1995. Elasticity of minerals, glasses, and melts. In: Minerals Physics & Crystallography: A handbook of physical constants, p. 45-63., AGU Reference Shelf. ISBN 9780875908526.

[9] Barree, R.D., Gilbert, J.V., and Conway, M.W., 2009. Stress and Rock Property Profiling for Unconventional Reservoir Stimulation. Paper SPE 118703 presented at the 2009 SPE Hydraulic Fracturing Technology Conference, The Woodlands, Texas, 19-21 January.

[10] Becerra-Rondon, D.M., 2017. Integrated Geological Characterization at the bed scale of the Woodford Shale at the I-35 Outcrop, Southern Oklahoma. M.S. Thesis, University of Oklahoma, Norman, OK.

[11] Biot, M. A. 1941. General theory of three-dimensional consolidation. J. Appl. Phys. 12 (2): 155–164. https://doi.org/10.1063/1.1712886.

[12] Boyce, M.L., and Carr, T.R., 2009. Lithostratigraphy and Petrophysics of the Devonian Marcellus Interval in West Virginia and Southwestern Pennsylvania. Unconventional Energy Resources.

[13] Brandt, A.R., Yeskoo, T., McNally, S., Vafi, K., Cai, H., and Wang, M.Q., 2015. Energy Intensity and Greenhouse Gas Emissions from Crude Oil Production in the Bakken Formation: Input Data and Analysis Methods.

[14] Buller, D., and Dix, M.C., 2009. Petrophysical evaluation of the Haynesville Shale in northwest Louisiana and northeast Texas. Gulf Coast Geological Association of Geological Societies Transactions, 59, p. 127–143.

[15] Buller, D., 2010. Unconventional resources in US: PTTC Newsletter, 16 (2), p. 2.

[16] Bullin, K.A., and Krouskop, P.E., 2009. Compositional variety complicates processing plans for US shale gas. Oil and Gas Journal, 107 (10).

[17] Bustin, R., Bustin, A., Cui, A., Ross, D., Murthy Pathi, V., 2008a. Impact of Shale Properties on Pore Structure and Storage Characteristics. Paper SPE 119892 presented at Shale Gas Production Conference, Fort Worth, Texas, USA, 16-18 November.

[18] Debrick, C.S., 2017. Well Planning and Construction Haynesville Shale – East Texas. Devon Energy. https://www.epa.gov/sites/production/ files/documents/ wellplanningandconstructiontechniques.pdf

[19] Cermak, V., and Rybach, L., 1982. Thermal properties: Thermal conductivity and specific heat of minerals and rocks. In: G. Angeneister (Ed.), Landolt-Bornstein Zahlenwerte and Funktionen aus Naturwissenschaften und Technik, Neue Serie, Physikalische Eigenschaften der Gesteine. Springer Verlag, Berlin, Heidelberg and New York, V/1a, 305-343.

[20] Chun, K.H., 2013. Thermo-Poroelastic Fracture Propagation Modeling with Displacement Discontinuity Boundary Element Method. Doctoral dissertation. Texas A&M university.

[21] Coates, J., 2008. Shallow Woodford Shale Gas Play in NE Oklahoma. Oklahoma Gas Shale Conference, October 22nd.

[22] Cheng, A. H.-D. 2016. Poroelasticity. Cham, Switzerland: Springer International.

[23] Cho, Y., Ozkan, E., and Apaydin, O.G., 2013. Pressure-Dependent Natural-Fracture Permeability in Shale and Its Effect on Shale-Gas Well Production. Society of Petroleum Engineers. Doi:10.2118/159801-PA.

[24] Cluff, R.M., Shanley, K.W., and Miller, M.A., 2007. Three things we thought we knew about shale gas but were afraid to ask, in AAPG Annual Convention Abstracts, 16, p. 5.

[25] Comer, J.B., 2005. "Facies Distribution and Hydrocarbon production potential of Woodford Shale in the Southern Midcontinent", in Cardott, B.J. [ed], Unconventional energy resources in the southern Midcontinent, 2004 symposium: Oklahoma Geological Survey Circular 110, p. 51-62.

[26] Cornwall, C. K. 1990. Core preservation—An alternative approach." In Proc., Society of Core Analysts Conf. New Brunswick, Canada: Society of Core Analysts.

[27] Curtis, M.E., Cardott, B.J., Sondergeld, C.H., and Rai, C.S., 2012. The development of organic of porosity in the Woodford Shale as a function of thermal maturity. Paper SPE 160158 presented at the annual Technical Conference and Exhibition, 8-10 October, San Antonio, Texas.

[28] Dadashpour, M., Ciaurri, D.E., Kleppe, J., and Landrø, M., 2009. Porosity and permeability estimation by integration of production and time-lapse near and far offset seismic data. Journal of Geophysics and Engineering, 6(4).

[29] Detournay, E., and Cheng, A.H.D., 1993. Fundamentals of poroelasticity. Chap. 5 in Vol. 2 of Comprehensive rock engineering: Principles, practice, and projects, edited by C. Fairhurst, 113–171. Oxford, UK: Pergamon Press.

[30] Dewers, T., Heath, J., Sanchez, M., 2019, Shale: Subsurface Science and Engineering, Americal Geophysical Union, ISBN: 978-1-119-06668-2 October 2019

[31] Dix, M., Spain, D., Walling, C., Sano, J., Casarta, N., and Richardson, A., 2010. Stratigraphy and depositional dynamics of the Haynesville-Bossier sequence: Inferences from whole-rock elemental data. AAPG Annual Convention and Exhibition, April 11–14, New Orleans, Louisiana.

[32] Dixon, D., Gray, M., Lingnau, B., Grahan, J., and Campbell, S., 1993. Thermal expansion testing to determinate the influence and pore water structure on water

flow through dense clays. 46th Canadian Geotechnical conference, Saskatoon, p. 177-184.

[33] Schlumberger, 2017. ECLIPSE technical description manual.

[34] EIA, 2016. https://www.eia.gov/maps/images/shale_gas_lower48.pdf

[35] Ettensohn, F., and Barron, L., 1981. Tectono-climatic model for origin of Devonian- Mississippian black gas shales of east-central United States: AAPG Bulletin, 65, p. 1-83.

[36] Ezekwe, N. 2011. Petroleum Reservoir Engineering Practive. Prentice Hall.

[37] François, B., 2008. Thermo-plasticity of fine-grained soils at various saturation states: Application to nuclear waste disposal. Ph.D. thesis. Soil Mechanics Laboratory, EPFL, Lausanne, Switzerland.

[38] Galvis-Portilla, H.A., 2017. Detailed Lithostratigraphic Characterization and Sequence Stratigraphy of a complete Woodford Shale Outcrop Section in Southern Oklahoma. Master's thesis, University of Oklahoma.

[39] Gaswirth, S.B., Marra, K.R., Cook, T.A., Charpentier, R.R., Gautier D.L., Higley D.K., Klett T.R., Lewan, M.D., Lillis, P.G., Schenk C.J., Tennyson, M.E., and Whidden, K.J., 2013. Assessment of the undiscovered oil resources in the Bakken and Three Forks Formations, Williston Basin Province, Montana, North Dakota, and South Dakota, 2013. U.S. Geological Survey Fact Sheet 2013-3013, p. 4.

[40] George, D.L., Bowles, E.B., 2011. Shale gas measurement and associated issues. Pipeline and Gas Journal, 238 (7).

[41] Ghosh S., 2017. Integrated studies on Woodford Shale natural fracture attributes, origin, and their relation to hydraulic fracturing. Ph.D. Dissertation, University of Oklahoma. https://doi.org/10.13140/RG.2.2.15739.82722

[42] Ghosh, S., Bontempi, C.P., Hooker, J.N., and Slatt, R.M., 2018a. High-resolution stratigraphic characterization of natural fracture attributes in the Woodford Shale, Arbuckle Wilderness and US-77D Outcrops, Murray County, Oklahoma. Interpretation, 6 (1), p. SC29–SC41. https://doi.org/10.1190/int-2017-0056.1

[43] Ghosh, S., Galvis-Portilla, H.A., Klockow, C.M., and Slatt, R.M., 2018b. An application of outcrop analogues to understanding the origin and abundance of natural fractures in the Woodford Shale. Journal of Petroleum Science and Engineering, 164 (2018), p. 623–639. https://doi.org/10.1016/j.petrol.2017.11.073

[44] Ghosh, S., and Slatt, R.M., 2019. Tectonic joint size, abundance, and connectivity: Examples from Woodford Shale and Hunton Limestone, 2019. The Shale Shaker, J. Okla. City Geol. Soc. 70 (3), 112-136

[45] Ghosh, S., Busetti, S., Slatt, R.M., 2019. Analysis and prediction of stimulated reservoir volumes through hydraulic fracturing: Examples from western Arkoma Basin. Journal of Petroleum Science and Engineering, 182 (2019), 106338. https://doi.org/10.1016/j.petrol.2019.106338

[46] Gilliam, T. M., & Morgan, I. L. (1987). Shale: Measurement of thermal properties (No. ORNL/TM-10499). Oak Ridge National Lab., TN (USA).

[47] Gupta, N., and Mishra, B,, 2017 "Creep Characterization of Marcellus Shale." Paper presented at the 51st U.S. Rock Mechanics/Geomechanics Symposium, San Francisco, California, USA, June 2017.

[48] Han, H.X., and Yin, S, 2018. Determination of in-situ stress and geomechanical properties from borehole deformation. Energies, 11, p. 131.

[49] Hair, T.J., 2014. Constructing a geomechanical model of the Woodford Shale, Cherokee Platform, Oklahoma, USA: effects of confining stress and rock strength on fluid flow. Department of Geology, Energy, and the Environment. Master's thesis, Texas Christian University.

[50] Havens, J., 2012. Mechanical properties of the Bakken Formation. Master's thesis, Colorado School of Mines.

[51] Hall, J.D., 2004. The Barnett Shale: An Unconventional Gas Play in the Fort Worth Basin – Now the Largest Gas Field in the State of Texas. Depositional Processes and Reservoir Characteristics of Siltstones, Mudstones, and Shales. Society for Sedimentary Geology.

[52] Hall, C.D., 2010. A comparison of gas shale reservoir properties-Muskwa, Marcellus, Barnett, Montney, Haynesville, and Eagle Ford. 4th B.C. Unconventional Gas Technical Forum, April 9, Victoria, British Columbia.

[53] Harper, J.A., 1999. Devonian, in Shultz, C.H., ed., The geology of Pennsylvania: Pennsylvania Bureau of Topographic & Geologic Survey and Pittsburgh Geological Society, p. 108-127.

[54] Harris, N.B., 2015. Shale Velocity and Density as Functions of TOC and Thermal Maturity: Upper Devonian Woodford Shale, Permian Basin, Texas. AAPG Annual Convention and Exhibition, Denver, CO., May 31 - June 3.

[55] Harrington, J., Whyte, C., Muehlenbachs, K., and Darrah T., 2015. Using Noble Gas and Hydrocarbon Gas Geochemistry to Source the Origin of Fluids in the Eagle Ford Shale of Texas, USA. Search and Discovery Article #41710.

[56] Hass, W.H., and Huddle, J.W., 1965. Late Devonian and Early Mississippian age of the Woodford Shale in Oklahoma as determined by conodonts, in Geological Survey research: U.S. Geological Survey Professional Paper 525-D, p. 125-132.

[57] He, Z., 2011. Flow of Gas and Water in Hydraulically Fractured Shale Gas Reservoirs. https://www.epa.gov/sites/production/files/documents/flowofgasandwaterinhfshalegasreservoirs.pdf

[58] Heller, R., Vermylen, J., and Zoback, M., 2014. Experimental investigation of matrix permeability of gas shales. AAPG Bulletin, 98(5), p. 975–995.

[59] Henry, J.D., 1982. Stratigraphy of the Barnett Shale (Mississippian) and associated reefs in the northern Fort Worth Basin, in Martin, C.A., ed., Petroleum geology of the Fort Worth Basin and Bend Arch area: Dallas Geological Society, Dallas, Texas, p. 157-177.

[60] Hester, T.C., and Schmoker, J.W., 1985. Selected Physical Properties Bakken Formation, North Dakota and Montana Part of the Williston Basin. U.S. Geological Survey.

[61] Hill, R.J., Jarvie, D.M., Zumberge, J., Henry, M., and Pollastro, RM, 2007. Oil and gas geochemistry and petroleum systems of the Fort Worth Basin. AAPG Bulletin, 91 (4), p. 445-473. https://doi.org/10.1306/11030606014

[62] Hill, R., 1952. The elastic behavior of a crystalline aggregate. Proceedings of the Physical Society, 65(5), p. 349. https://doi.org/10.1088/0370 -1298/65/5/307.

[63] Horsfield, B., Muscio, G.P., Grice, K., Primio, R., Kuhn, P., and Maslen E., 2008. Gas Generation and Retention in the Bakken Shale, Williston Basin. Search and Discovery Article #40330.

[64] Hosseini Boosari, SS., Aybar, U., Eshkalak, M.O., 2016. Unconventional resource's production under desorption-induced effects, Petroleum, Volume 2, Issue 2, 2016, Pages 148-155.

[65] Itasca Consulting Group. 2002. FLAC3D: Fast Lagrangian analysis of continua in three dimensions. Minneapolis: Itasca Consulting Group.

[66] Jarrahian, A., and Heidaryan, E., 2014. A simple correlation to estimate natural gas thermal conductivity. Journal of Natural Gas Science and Engineering, 18 (2014), p. 446-450.

[67] Jarvie, D.M., Hill, R.J., Ruble, T.E., and Pallastro, R.M., 2007. Unconventional shale-gas systems: The Mississippian Barnett Shale of north-central Texas as one model for thermogenic shale-gas assessment. AAPG Bulletin, 91(4), p. 475–499. DOI:10.1306/12190606068.

[68] Jiang, M., Spikes, K.T., 2013. Estimation of reservoir properties of the Haynesville Shale by using rock-physics modelling and grid searching, *Geophysical Journal International*, 195(1), p. 315–329. https://doi.org/10.1093/gji/ggt250.

[69] Jin, Z., Li, W., Jin, C., Hambleton, J., and Cusatis, G., 2017. Elastic, strength, and fracture properties of Marcellus shale. International Journal of Rock Mechanics and Mining Sciences. 109. 10.1016/j.ijrmms.2018.06.009.

[70] Klein C., Hurlbut Jr.C.S., 1985. Manual of mineralogy. (20th edition), John Wiely & Sons, ISBN 047180580, New York.

[71] Kowan, J., and Ong, S.H., 2016. Wellbore Stability: Special Considerations for the Marcellus Shale. Search and Discovery Article #80533.

[72] Kane, J., 2006. Petrophysical Characterization of the Barnett Shale: Progress Report. Bureau of Economic Geology, PBGSP Annual Meeting, February 27-28.

[73] Kareem, L.A., Iwalewa, T.M., Omeke, J.E., 2014. Isobaric specific heat capacity of natural gas as a function of specific gravity, pressure and temperature. Journal of Natural Gas Science and Engineering, 19 (2014), p. 74-83.

[74] Kingery, W.D., Bowen, H.K., Uhlmann, D.R., 1976. Introduction to ceramics, 2nd edition. Wiley, New York.

[75] Ko, L.C., Loucks, R.G., Ruppel, S.C., Zhang, T., Peng, S., 2017. Origin and characterization of Eagle Ford pore networks in the south Texas Upper Cretaceous shelf.

[76] Kohlruss, D., and Stamatinos, K., 2014. Preliminary bulk density mapping of the Upper and Lower Bakken Member shales of southeastern Saskatchewan: a potential indicator for oil generation and expulsion; in Summary of investigations 2014, Volume 1, Saskatchewan Geological Survey, Sask. Ministry of the Economy, Misc. Rep. 2014-4.1, Paper A-2, p. 7.

[77] Kort, E.A., Smith, M.L., Murray, L.T., Gvakharia, A., Brandt A.R., Peischl, J., Ryerson, T.B., Sweeney, C., and Travis, K., 2016. Fugitive emissions from the Bakken shale illustrate role of shale production in global ethane shift. Geophysics Research Letter, 43, p. 4617–4623. Doi: 10.1002/2016GL068703.

[78] Kneafsey, T. J., Lu, H., Winter, W., Boswell R., Hunter R., Collet T. S., 2011. Examination of core samples from the Mount Elbert Gas hydrate stratigraphic test well, Alaska North Slope: Effects of retrieval and preservation. Mar. Pet. Geol. 28 (2): 381–393.

[79] LeCompte, B., Franquet, J.A., and Jacobi, D., 2009. Evaluation of Haynesville Shale Vertical Well Completions With a Mineralogy Based Approach to Reservoir Geomechanics. Society of Petroleum Engineers. Doi:10.2118/124227-MS.

[80] Lee, A.L., Gonzalez, M.H., and Eakin, B.E., 1966. The viscosity of natural gases. Journal of Petroleum Technology, 18(8), p. 997–1000. https://doi.org/10.2118/1340-PA.

[81] Lee, M.W., 2004. Elastic velocities of partially gas saturated unconsolidated sediments. Marine of Petroleum Geology, 21, p. 641-650.

[82] Lora, V.R., Ghazanfari, E., and Izquierdo, E.A., 2016. Geomechanical Characterization of Marcellus Shale. Rock Mechanics and Rock Engineering, 49(6), p. 3403-3424.

[83] Loucks, R.G., Reed, R.M., Ruppel, S.C., and Hammes, U., 2012. Spectrum of pore types and networks in mudrocks and a descriptive classification for matrix-related mudrock pores. AAPG Bulletin, 96 (6), p. 1071-1098.

[84] Martin, E.A., 2017. Rock physics model for the characterization of organic-rich shale from elastic properties. Rock evaluation and Wellbore stability. October 8th, 2017.

[85] McCullough, B.J., and Slatt, R.M., 2014. Stratigraphic Variability of the Woodford Shale across Oklahoma. Search and Discovery Article#80417

[86] McKeon, M., 2011. Horizontal Fracturing in Shale Plays. http://www.thepttc.org/workshops/eastern_062111/eastern_062111_McKeon.pdf.

[87] McKean, H.P., 1967. Propagation of chaos for a class of non-linear parabolic equations. In Vol. 7 of Lecture series in differential equations, 41–57.Washington, DC: Catholic University.

[88] McKinstry, H.A., 1965. Thermal expansion of clay minerals. American Mineralogist, 50, p. 212-222.

[89] McTigue, D.F. 1986. Thermoelastic response of fluid-saturated porous rock. J. Geophys. Res. 91 (B9): 9533–9542. https://doi.org/10.1029/JB091iB09p09533.

[90] Midttomme, K., Roaldset, E., Aagaard, P., 1998. Thermal conductivity of selected claystones and mudstones from England. Clay Minerals, 33, p. 131-145.

[91] Mokhtari M. 2015. Characterization of anisotropy in organic-rich shales: shear and tensile failure, wave velocity, matrix and fracture permeability. PhD Dissertation. Colorado School of Mines.

[92] Mokhtari, M., Honarpour, M.M.M., Tutuncu, A.N., Boitnott, G.N., 2014. Acoustical and Geomechanical Characterization of Eagle Ford Shale-Anisotropy, Heterogeneity, and Measurement Scale. Society of Petroleum Engineers. Doi:10.2118/170707-MS.

[93] Monfared, S.K., 2015. Microporoelastic Modeling of Organic-Rich Shales. Master's thesis, Massachusetts Institute of Technology.

[94] Montgomery, S.L., Jarvie, D.M., Kent, A., Bowker, K.A., and Pollastro, R.M., 2005. Mississippian Barnett Shale, Fort Worth Basin, north-central Texas: Gas-shale play with multi-trillion cubic foot potential. AAPG Bulletin, 89(2), p. 155–175.

[95] Milkov, A.V., Schwietzke, S., Allen, G., Sherwood, O.A., Etiope G. (2020) Scientific Reports (Nature Publisher Group); London Vol. 10, Iss. 1, (2020). DOI:10.1038/s41598-020-61035-w

[96] Okiongbo, K.S., Aplin, A.C., Larter, S.R., 2005. Changes in Type II Kerogen Density as a Function of Maturity: Evidence from the Kimmeridge Clay Formation. Energy Fuels, 2005, 19 (6), p. 2495–2499.

[97] Onishchenko, Y.V., Sitnov, S.A., Ivanova, A.G., Vakhin, A.V., and Nurgaliev, D.K., 2017. Destruction of Kerogen in the presence of pyrite and cobalt-based catalyst. Indian Journal of science and technology, 10 (1).

[98] Ortega, J.A., 2010. Microporomechanical Modeling of Shale. PhD Dissertation, Massachusetts Institute of Technology.

[99] Ostadhassan M. 2013. Geomechanics and elastic anisotropy of the Bakken Formation, Williston Basin. PhD Dissertation. University of North Dakota.

[100] Palciauskas, V. V., and P. A. Domenico. 1982. Characterization of drained and undrained response of thermally loaded repository rocks. Water Resour. Res. 18 (2): 281–290. https://doi.org/10.1029/WR018i002p00281.

[101] Perry, F.V., Kelley, R.E., Lugo, A.B., Birdsell, S.M., Dobson, P., Houseworth, J.E., 2014. Database for Regional Geology, Phase 1– A Tool for informing Regional Evaluations of Alternative Geologic Media and Decision Making. Los Alamos National Laboratory and Lawrence Berkeley National Laboratory. Prepared for U.S. Department of Energy, Used Fuel Disposition Campaign.

[102] Peterson, A.J., 1996. Bakken and other Devonian-Mississippian Petroleum Source Rocks, Northern Rocky Mountains -Williston Basin: Depositional and Burial History and Maturity Estimations. Expanded Abstracts Volume: Rocky Mountain Section Meeting: AAPG, 1996.

[103] Pollastro, R.M., Hill, R.J., Ahlbrandt, T.S., Charpentier R.R., Cook T.A., Klett T.R., Henry M.E., and Schenk C.J., 2004. Assessment of undiscovered oil and gas resources of the Bend arch-Fort Worth Basin province of northcentral Texas and southwestern Oklahoma: National Assessment of Oil and Gas Fact Sheet-U.S. Geological Survey FS2004-3022: http://pubs.usgs.gov/fs/2004/3022/fs-2004-3022.pdf.

[104] Prasad, U., Franquet, J., Gonzalez, H. P., Moronkeji, D., Shouse, R., McGlynn, I., and Clawson, C.F., 2016. Integrated Evaluation of Haynesville Shale with Special Emphasis on Anisotropy. Paper presented at the 50th U.S. Rock Mechanics/Geomechanics Symposium, Houston, Texas, June 2016.

[105] Redlinger, M, 2015. Drilling Down the Bakken Learning Curve. Colorado School of Mines Division of Economics and Business. https://ideas.repec.org/p/mns/wpaper/wp201504.html

[106] Reuss, A., 1929. Berechnung der Fließgrenze von Mischkristallen auf Grund der Plastizitätsbedingung für Einkristalle. Journal of Applied of Mathematics and Mechanics, 9(1), p. 49–58.

[107] Rice, J. R., and M. P. Cleary. 1976. Some basic stress-diffusion solutions for fluid saturated elastic porous media with compressible constituents. Rev. Geophys. Space Phys. 14 (2): 227–241. https://doi.org/10.1029 /RG014i002p00227.

[108] Roen, J.B. and Walker, B.J. (eds.), 1996. The atlas of major Appalachian gas plays. Morgantown, WV, West Virginia Geological and Economic Survey Publication 25, 1996, 201 p.

[109] Rowan E.L., Engle M.A., Kraemer T.F., Schroeder K.T., Hammack R.W., and Doughten M.W., 2014. Geochemical and isotopic evolution of water produced from Middle Devonian Marcellus shale gas wells, Appalachian basin, Pennsylvania. AAPG Bulletin, 99(2), p. 181–206.

[110] Rutqvist, J., Rinaldi A.P., Cappa, F., Moridis, G.J., 2013. Modeling of fault reactivation and induced seismicity during hydraulic fracturing of shale-gas reservoirs. J Petrol Sci Eng 107:31–44.

[111] Schmoker, J.W., Quinn J.C., Crovelli R.A., Nuccio V.F., and Hester T.C., 1996. Production characteristics and resource assessment of the Barnett shale continuous (unconventional) gas accumulation, Fort Worth Basin, Texas, US. Department of the Interior. US. Geological Survey.

[112] Sierra, R., Tran, M.H., Abousleiman, Y.N., and R.M. Slatt, 2010. Woodford Shale Mechanical Properties And the Impacts of Lithofacies." Paper presented at the 44th U.S. Rock Mechanics Symposium and 5th U.S.-Canada Rock Mechanics Symposium, Salt Lake City, Utah, June 2010.

[113] Skauge, A., Fuller, N., and Hepler, L.G., 1983. Specific heats of clay minerals: Sodium and calcium kaolinites, sodium and calcium montmorillonites, illite, and attapulgite. Thermochimica Acta, 61, p. 139-145.

[114] Skempton, A. W. 1954. The pore pressure coefficients A and B. Geotechnique 4 (4):143–147. https://doi.org/10.1680/geot.1954.4.4.143.

[115] Slatt, R.M., Buckner, N., Abousleiman, Y., Sierra, R., Philp P.R., and Miceli-Romero A., 2012. Outcrop-behind Outcrop (Quarry): Multiscale Characterization of the Woodford Gas Shale, Oklahoma.

[116] Sone, H. 2012. Mechanical properties of shale gas reservoir rocks, and its relation to the in-situ stress variation observed in shale gas reservoirs. PhD Dissertation. Stanford University.

[117] Sone, H., and Zoback, M.D., 2014. Viscous relaxation model for predicting least principal stress magnitudes in sedimentary rocks, Journal of Petroleum Science and Engineering, 124 (2014), p. 416-431.

[118] Sondergeld, C.H., Newsham, K.E., Comisky, J.T., Rice, M.C., and Rai, C.S., 2010. Petrophysical considerations in evaluating and producing shale gas resources. In: Proceedings of unconventional gas conference, Pittsburgh; 23–25 February.

[119] Spain, D.R., and Anderson, G.A., 2010. Controls on reservoir quality and productivity in the Haynesville Shale, northwestern Gulf of Mexico Basin: Gulf Coast Association of Geological Societies Transactions, 60, p. 657–668.

[120] Stoneburner, R.K., 2017. The Eagle Ford Shale Field in the Gulf Coast Basin of South Texas, U.S.A. A “Perfect” Unconventional Giant Oil Field. Memoir 113: Giant Fields of the decade 2000-2010. DOI: 10.1306/13572003M1133682.

[121] Stidham, J., 2011. Chesapeake Energy: Eagle Ford Shale Overview. AADE Operator's Forum Oklahoma City Chapter.

[122] Suppachoknirun, T., and Tutuncu, A.N., 2017. Hydraulic Fracturing and Production Optimization in Eagle Ford Shale Using Coupled Geomechanics and Fluid Flow Model. Rock Mechanics and Rock Engineering, 50(12), p. 3361-3378.

[123] Taghichian, A., Hashemolhosseini, H., Zaman, M., Yang, Z.Y. Porothermoelastic Response and Damage Potential of Tripping Unconventional Cores from Six Different Shale Plays. International Journal of Geomechanics Volume 19 Issue 1 - January 2019.

[124] Taylor, T., 2013. Lithostratigraphic and Petrophysical Analysis of the Middle Devonian Marcellus Shale at the Mamont Prospect, Westmoreland County, Pennsylvania. Master's Thesis, Clemson University.

[125] Terzaghi, K., 1923. Die Berechnung der Durchlassigkeitsziffer des Tones aus Dem Verlauf der Hidrodynamichen Span nungserscheinungen. Sitz. Akad. Wissen. Wien Math. Naturwiss. Kl. Abt. IIa 132: 125–138.

[126] U.S. EIA, 2014a. Independent statistics and analyses. Updates to the EIA Eagle Ford Play Maps. December 2014a. https://www.eia.gov/maps/pdf/EIA%20Eagle%20Ford%20Play%20update%2012-29-14.pdf

[127] U.S. EIA, 2014b. Bakken fuels north Dakota's oil production growth. https://www.eia.gov/todayinenergy/detail.php?id=17391

[128] U.S. EIA, 2017a. Marcellus Shale Play: Geology review. https://www.eia.gov/maps/pdf/MarcellusPlayUpdate_Jan2017.pdf

[129] US EIA, 2017b. Independent statistics and analyses. Haynesville shale gas production increases to highest levels since end of 2013. https://www.eia.gov/todayinenergy/detail.php?id=33512.

[130] Vanorio, T., Prasad, M., and Nur, A., 2003. Elastic properties of dry clay mineral aggregates, suspensions, and sandstones. Geophysics Journal International, 155(1), p. 319-326.

[131] Vermylen, J.P., 2011. Geomechanical studies of the Barnett shale, Texas, USA. Doctoral dissertation, Stanford University.

[132] Vernik, L., 1993. Microcrack-induced versus intrinsic elastic anisotropy in mature HC-source shale. Geophysics, 58, (11), p. 1703-1706.

[133] Voigt,W., 1928. Lehrbuch der kristallphysik, 739. Stuttgart: Teubner.

[134] Wang, Y., Liang, H., Zhang, M, and Yang, Z., 2017. Study on correlation between mineralogical composition and elastic modulus of clay rock for geological repository at home and abroad. Advances in Engineering Research (AER), 135.

[135] Wang, Z., Wang, H., and Cates, M.E., 2001. Effective elastic properties of solid clays, geophysics, 66, p. 428-440, 2001.

[136] Wang, F.P., and Hammes, U., 2010. Key petrophysical factors affecting fluid flow and production in the geopressured. Haynesville Shale: World Oil, 231 (6), p. 4.

[137] Wang, F.P., and Hammes U., 2013. Overview of Haynesville Shale Properties and Production. DOI: 10.1306/13441848M1053527

[138] Wang, G. and T.R., Carr, 2013. Organic-rich Marcellus Shale lithofacies modeling and distribution pattern analysis in the Appalachian Basin. AAPG Bulletin, 97(12).

[139] Waples, D.W., and Waples, J.S., 2004. A review and evaluation of specific heat capacities of rocks, minerals, and subsurface fluids. Part 1: Minerals and non-porous rocks. Natural Resources Research, 13(2).

[140] Webster, R.L., 1984. Petroleum source rocks and stratigrapy of the Bakken Formation in North Dakota. Hydrocarbon Source Rocks of the Greater Rocky Mountain Region.

[141] Wickstrom, C.W., 2008. Woodford Shale Gas in Oklahoma. Search and Discovery Article #110068.

[142] Willis, M., 2013. Upscaling Anisotropic Geomechanical Properties using Backus Averaging and Petrophysical Clusters in the Vaca Muerta Formation. Master's Thesis, Colorado School of Mines.

[143] Williams, K.E., 2012. The Permeability of Overpressure Shale Seals and of Source Rock Reservoirs is the Same. AAPG Annual Convention and Exhibition, Long Beach, California, 22-25 April.

[144] World oil. Shaletech/Haynesville, 2015. Systematic candidate selection improves Haynesville refracturing economic. Pages 67-71, posted with permission.

[145] Younes, A.I., Moore H., Suurmeyer, N., Smith P.R., and Sandstrom M., 2011. Development of mechanically layered Haynesville-Bossier Shale-Gas play. Search and Discovery Article #50460.

[146] Yu, W., and Sepehrnoori, K., 2013. Numerical Evaluation of the Impact of Geomechanics on Well Performance in Shale Gas Reservoirs. American Rock Mechanics Association 13-555.

[147] Zagorski, B., 2016. The Marcellus Play: A Look At Where We Are Today. SunTrust 11th Annual Appalachian Conference. Range Resources.

[148] Zagorski, W.A., Bowman, D.C., Emery, M., and Wrightstone, G.R., 2011. An overview of Some Key Factors Controlling Well Productivity in Core Areas of the Appalachian Basin Marcellus Shale Play. Search and Discovery Article #110147.

[149] Zagorski, W.A., Wrightstone, G.R., and Bowman, D.C., 2012. The Appalachian Basin Marcellus gas play: Its history of development, geologic controls on production, and future potential as a world-class reservoir, in J.A. Breyer, ed., Shale reservoirs -Giant resources for the 21st century: AAPG Memoir 97, p. 172-200.

[150] Zuo, L., Humbert, M., and Esling, C., 1992. Elastic properties of polycrystals in the Voigt-Reuss-Hill approximation. Journal of Applied Crystallography, 25, p. 751–755. https://doi.org/10.1107/S0021889892004874

[151] Zubizarreta, I., Byrne, M., Jimenez, M.A., Rojas, E., Sorrentino, Y., and Velazco, M.A., 2011. Pore pressure evolution and core damage: A computational fluid dynamic approach. In Proc., Int. Symp. of the Society of Core Analysts Annual Meeting. New Brunswick, Canada: Society of Core Analysts.

Appendix A. Analytical solution of a poroelastic cylinder

Poroelastic rock cylinder can be subjected to different modes of application of boundary conditions, such as pore pressure, flow rate, hydrostatic and deviatoric stress for drained and undrained conditions. However, for the case of a tripping core, only two modes of pore pressure and radial stress application suffice for understanding the behavior of a tripping poroelastic core. Having time-dependent boundary conditions is also a privilege. Abousleiman and Cui (1998) have solved this problem and presented the pore pressure and stress fields in Laplace domain as follows:

$$\tilde{p} = \frac{M_{11}}{\alpha} A_1 I_0(\xi) - 2\alpha M A_2 \tag{A-1}$$

$$\frac{\tilde{\sigma}_{rr}}{2G} = -A_1 \frac{I_1(\xi)}{\xi} + \frac{M_{11} + M_{12} + 2\alpha^2 M}{2G} A_2 \tag{A-2}$$

$$\frac{\tilde{\sigma}_{\theta\theta}}{2G} = -A_1 \left(I_0(\xi) - \frac{I_1(\xi)}{\xi} \right) + \frac{M_{11} + M_{12} + 2\alpha^2 M}{2G} A_2 \tag{A-3}$$

For mode I loading, at $r = R$:

$$p = p_0(t) \qquad A_1 = \tilde{p}_0 \frac{M_{11} + M_{12} + 2\alpha^2 M}{2G} \frac{\beta}{C_1 I_1(\beta)} \tag{A-4}$$

$$\sigma_{rr} = 0 \qquad A_2 = \frac{\tilde{p}_0}{C_1} \tag{A-5}$$

$$\tau_{r\theta} = 0 \qquad C_1 = \frac{M_{11} + M_{12} + 2\alpha^2 M}{2G} \frac{M_{11}}{\alpha} \frac{\beta I_0(\beta)}{I_1(\beta)} - 2\alpha M \tag{A-6}$$

For mode II loading, at $r = R$:

$$p = 0 \qquad A_1 = -\frac{\tilde{P}_0}{G C_3} \frac{\alpha^2 M}{M_{11} I_0(\beta)} \tag{A-7}$$

$$\sigma_{rr} = -P_0(t) \qquad A_2 = -\frac{\tilde{P}_0}{2 G C_3} \tag{A-8}$$

$$\tau_{r\theta} = 0 \qquad C_3 = \frac{M_{11} + M_{12} + 2\alpha^2 M}{2G} - \frac{2\alpha^2 M}{M_{11}} \frac{I_1(\beta)}{\beta I_0(\beta)} \tag{A-9}$$

Appendix B. Analytical solution of a porothermoelastic core problem with constant boundary conditions

The analytical solution of a porothermoelastic core problem was solved by Cheng (2016). The initial condition is given as $T = 0$ and $p = 0$. The boundary conditions for the problem of a step rise in temperature on the cylinder surface are as follows:

$$\sigma_{rr} = 0;\ p = 0; T = T_1; at\ r = r_0$$

By solving the governing equations with the associated boundary and initial conditions, different fields are

$$\tilde{T} = C_1 I_0\left(\lambda_1\sqrt{s}r\right) + C_2 I_0\left(\lambda_2\sqrt{s}r\right) - \frac{2\left(\alpha_d S + \alpha\alpha_p S_a\right)}{SS_a\left(1-\alpha_p\alpha_e\right)}\tilde{A}_1(s) \tag{B-1}$$

$$\tilde{p} = \frac{C_1\left(c - c_a - C_Q\right)I_0\left(\lambda_1\sqrt{s}r\right)}{2c\alpha_p} + \frac{C_2\left(c - c_a + C_Q\right)I_0\left(\lambda_2\sqrt{s}r\right)}{2c\alpha_p} - \frac{2(\alpha S_a + \alpha_d\alpha_e S)}{SS_a\left(1-\alpha_p\alpha_e\right)}\tilde{A}_1(s) \tag{B-2}$$

$$\tilde{\sigma}_{rr} = -2\eta\frac{1}{r^2}\int r\tilde{p}(r,t)dr - 2\eta_d\frac{1}{r^2}\int r\tilde{T}(r,t)dr + \frac{2G}{1-2\nu}\tilde{A}_1(s) \tag{B-3}$$

$$\tilde{\sigma}_{\theta\theta} = 2\eta\frac{1}{r^2}\int r\tilde{p}(r,t)dr + 2\eta_d\frac{1}{r^2}\int r\tilde{T}(r,t)dr - 2\eta\tilde{p} - 2\eta_d\tilde{T} + \frac{2G}{1-2\nu}\tilde{A}_1(s) \tag{B-4}$$

Utilizing the temperature and pore pressure boundary conditions, C_1 and C_2 are obtained as:

$$\begin{aligned}C_1 = &\frac{1}{2sC_Q SS_a\left(1-\alpha_p\alpha_e\right)I_0\left(\lambda_1\sqrt{s}r_0\right)}\\ &\times\left\{2s\left[\left(c - c_a + C_Q\right)\left(S\alpha_d + S_a\alpha\alpha_p\right) - 2c\alpha_p\left(S_a\alpha + S\alpha_d\alpha_p\right)\right]\tilde{A}_1(s)\right.\\ &\left.+ SS_a T_1\left(c - c_a + C_Q\right)\left(1-\alpha_p\alpha_e\right)\right\}\end{aligned}$$

$$\begin{aligned}C_2 = &-\frac{1}{2sC_Q SS_a\left(1-\alpha_p\alpha_e\right)I_0\left(\lambda_2\sqrt{s}r_0\right)}\\ &\times\left\{2s\left[\left(c - c_a - C_Q\right)\left(S\alpha_d + S_a\alpha\alpha_p\right) - 2c\alpha_p(S_a\alpha + S\alpha_d\alpha_e)\right]\tilde{A}_1(s)\right.\\ &\left.+ SS_a T_1\left(c - c_a - C_Q\right)\left(1-\alpha_p\alpha_e\right)\right\}\end{aligned}$$

The integrals are:

$$\int r\tilde{T}(r,s)dr = \frac{C_1 r I_1\left(\lambda_1\sqrt{s}r\right)}{\lambda_1\sqrt{s}} + \frac{C_1 r I_1\left(\lambda_2\sqrt{s}r\right)}{\lambda_2\sqrt{s}} - \frac{r^2\left(\alpha_d S + \alpha\alpha_p S_a\right)}{SS_a\left(1-\alpha_p\alpha_e\right)}\tilde{A}_1(s)$$

$$\begin{aligned}\int r\tilde{p}(r,s)dr = &\frac{\left(c - c_a - C_Q\right)C_1 r I_1\left(\lambda_1\sqrt{s}r\right)}{2c\alpha_p\lambda_1\sqrt{s}} + \frac{\left(c - c_a + C_Q\right)C_2 r I_1\left(\lambda_2\sqrt{s}r\right)}{2c\alpha_p\lambda_2\sqrt{s}}\\ &- \frac{r^2(\alpha S_a + \alpha_d\alpha_e S)}{SS_a\left(1-\alpha_p\alpha_e\right)}\tilde{A}_1(s)\end{aligned}$$

$$\begin{aligned}
\tilde{A}_1(s) = \frac{SS_aT_1(1-2\nu)\left(1-\alpha_p\alpha_e\right)}{D} & \\
\times \{\lambda_1\left(c-c_a-C_Q\right)&\left[\eta\left(c-c_a+C_Q\right)+2c\alpha_p\eta_d\right] \\
\times I_0\left(\lambda_1\sqrt{s}r_0\right)&I_1\left(\lambda_2\sqrt{s}r_0\right) \\
-\lambda_2\left(c-c_a+C_Q\right)&\left[\eta\left(c-c_a-C_Q\right)+2c\alpha_p\eta_d\right] \\
\times I_0\left(\lambda_2\sqrt{s}r_0\right)&I_1\left(\lambda_1\sqrt{s}r_0\right)\}
\end{aligned}$$

$$\begin{aligned}
D = 2s(1-2\nu)&\{\lambda_2\left[\left(c-c_a+C_Q\right)\left(\alpha_dS+\alpha\alpha_pS_a\right)-2c\alpha_p(\alpha S_a+\alpha_d\alpha_eS)\right] \\
&\times\left[\eta\left(c-c_a-C_Q\right)+2c\alpha_p\eta_d\right]I_0\left(\lambda_2\sqrt{s}r_0\right)I_1\left(\lambda_1\sqrt{s}r_0\right) \\
&-\lambda_1\left[\left(c-c_a-C_Q\right)\left(\alpha_dS+\alpha\alpha_pS_a\right)-2c\alpha_p(\alpha S_a+\alpha_d\alpha_eS)\right] \\
&\times\left[\eta\left(c-c_a+C_Q\right)+2c\alpha_p\eta_d\right]I_0\left(\lambda_1\sqrt{s}r_0\right)I_1\left(\lambda_2\sqrt{s}r_0\right)\} \\
&-4cC_Q\alpha_pr_0\lambda_1\lambda_2s^{3/2}\{GSS_a\left(1-\alpha_p\alpha_e\right) \\
&+(1-2\nu)\left[\alpha_dS(\alpha_e\eta+\eta_d)+\alpha S_a\left(\eta+\alpha_p\eta_d\right)\right]\} \\
&\times I_0\left(\lambda_1\sqrt{s}r_0\right)I_0\left(\lambda_2\sqrt{s}r_0\right)
\end{aligned}$$

All the required variables are defined as follows:

Drained thermoelastic constitutive constant	$m_d=\frac{\rho c_d}{\tau_0}$	(B-5)
Adiabatic drained bulk modulus	$K_a=K+\frac{\alpha_d^2}{m_d}$	(B-6)
Adiabatic drained thermal storage coefficient	$S_a=\frac{m_d(3K_a+4G)}{3K+4G}$	(B-7)
Poroelastic effective stress coefficient in thermal diffusion equation	$\alpha_p=\frac{\beta_c}{S_a}$	(B-8)
Thermoelastic effective stress coefficient in pore pressure diffusion equation	$\alpha_e=\frac{\beta_c}{S}$	(B-9)
Storage coefficient (constant stress uniaxial strain)	$S=\frac{3K_u+4G}{M(3K+4G)}$	(B-10)
Drained thermoelastic effective stress coefficient	$\alpha_d=K\beta_d$	(B-11)
Thermoelastic stress coefficient	$\eta_d=\frac{\alpha_d(1-2\nu)}{2(1-\nu)}$	(B-12)

Appendix C. Formulation for determination of gas properties

In order to determine the properties of the gas in the pore spaces of a shale play, it is first required to determine the critical pressure and temperature of the gas mixture from the critical pressure and temperature of the gas constituents as methane to butane (C1 to C4), nitrogen (N_2), carbon dioxide (CO_2), etc. This can be performed by weight averaging of the gas constituents or with specific gravity of the gas (See Kareem et al., 2014). Thereafter, by determining four coefficients of A_z to D_z one can determine gas compressibility factor. It is also possible to numerically determine the gradient of gas compressibility factor with respect to pressure. After that, via this gradient, gas compressibility and bulk modulus are estimated. Finally, gas viscosity is calculated by determining the viscosity coefficients, A_μ to C_μ. It is worth mentioning that all these parameters are pressure and temperature dependent. Therefore, upon change in pore pressure or temperature these parameters also change.

$$Z = A_z + (1 - A_z) \times \exp(-B_z) + C_z \times p_{pr}^{D_z} \tag{C-1}$$

where,

$$A_z = 1.39(T_{pr} - 0.92)^{0.5} - 0.36T_{pr} - 0.101 \tag{C-1a}$$

$$B_z = p_{pr}(0.62 - 0.23T_{pr}) + p_{pr}^2\left[\frac{0.066}{T_{pr} - 0.86} - 0.037\right] + \frac{0.32p_{pr}^6}{exp(20.723(T_{pr} - 1)}) \tag{C-1b}$$

$$C_z = 0.132 - 0.32\log T_{pr} \tag{C-1c}$$

$$D_z = \exp(0.715 - 1.128T_{pr} + 0.42T_{pr}^2) \tag{C-1d}$$

Here, $T_{pr} = T/T_{pc}$ have both of temperatures in °R; $p_{pr} = p/p_{pc}$ have both pressures in psi; T_{pc}, p_{pc} are pseudo-critical temperature and pressure, respectively and T_{pr}, p_{pr} are the corresponding reduced ones.

In addition, specific gravity of the gas is determined as:

$$\gamma_g = (M_g/M_{air}) \tag{C-2}$$

where, M is molecular weight.

Gas density is determined as follows:

$$\rho_g = 0.0433p\gamma_g/ZT \tag{C-3}$$

The viscosity of the gas is determined by the following equation:

$$\mu_g = A_\mu \times 10^{-4}exp(B_\mu\rho_g^{C_\mu}) \tag{C-4}$$

where the coefficients are defined as follows:

$$A_\mu = \frac{(9.4 + 0.02M_g)T^{1.5}}{(209 + 19M_g + T)} \tag{C-4a}$$

$$B_\mu = 3.5 + 0.01M_g + \frac{986}{T} \tag{C-4b}$$

$$C_\mu = 2.4 - 0.2B_\mu \tag{C-4c}$$

Appendix D. Distribution curves for porothermomechanical properties of Marcellus shale

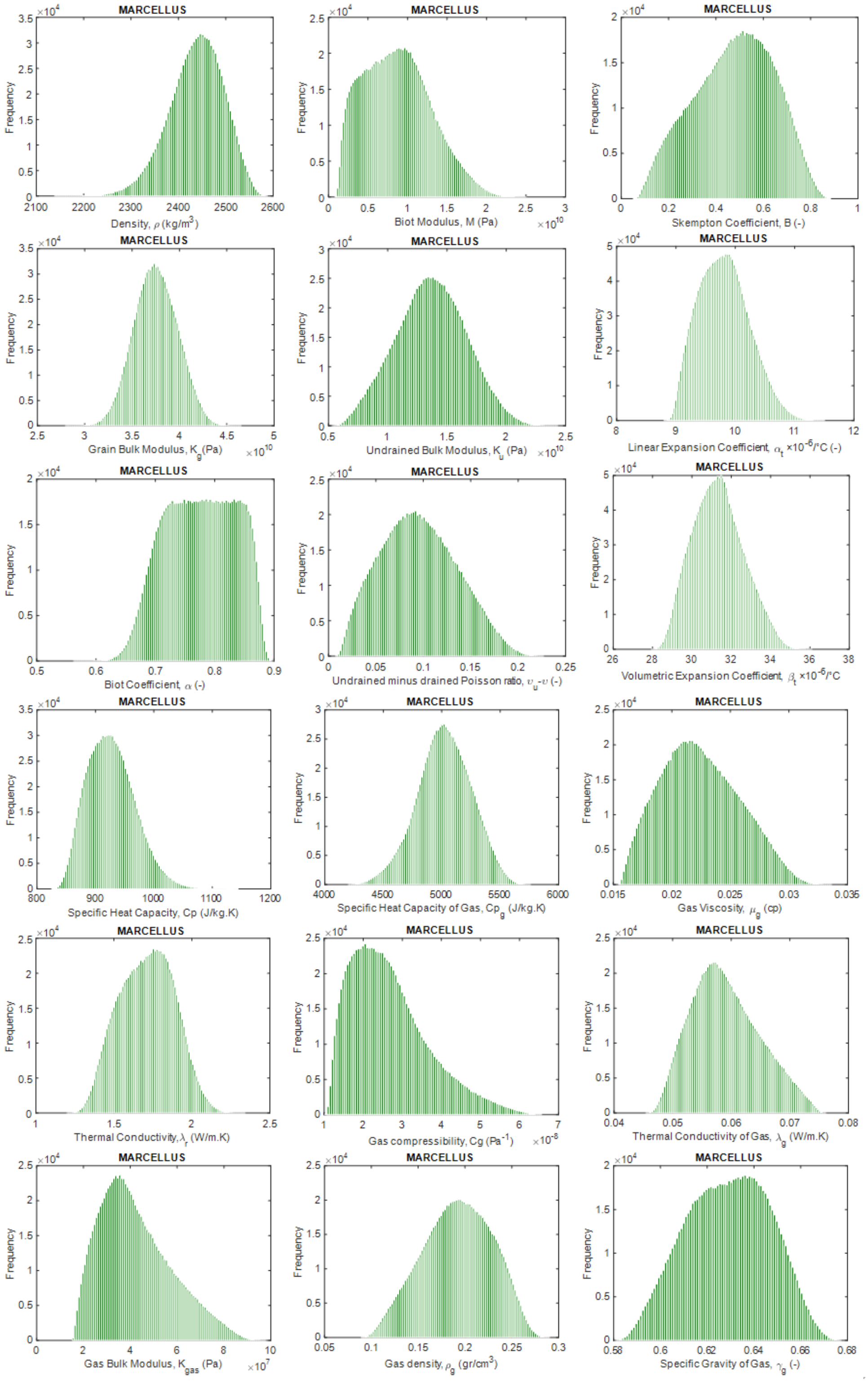

Appendix E. Distribution curves for porothermomechanical properties of Woodford shale

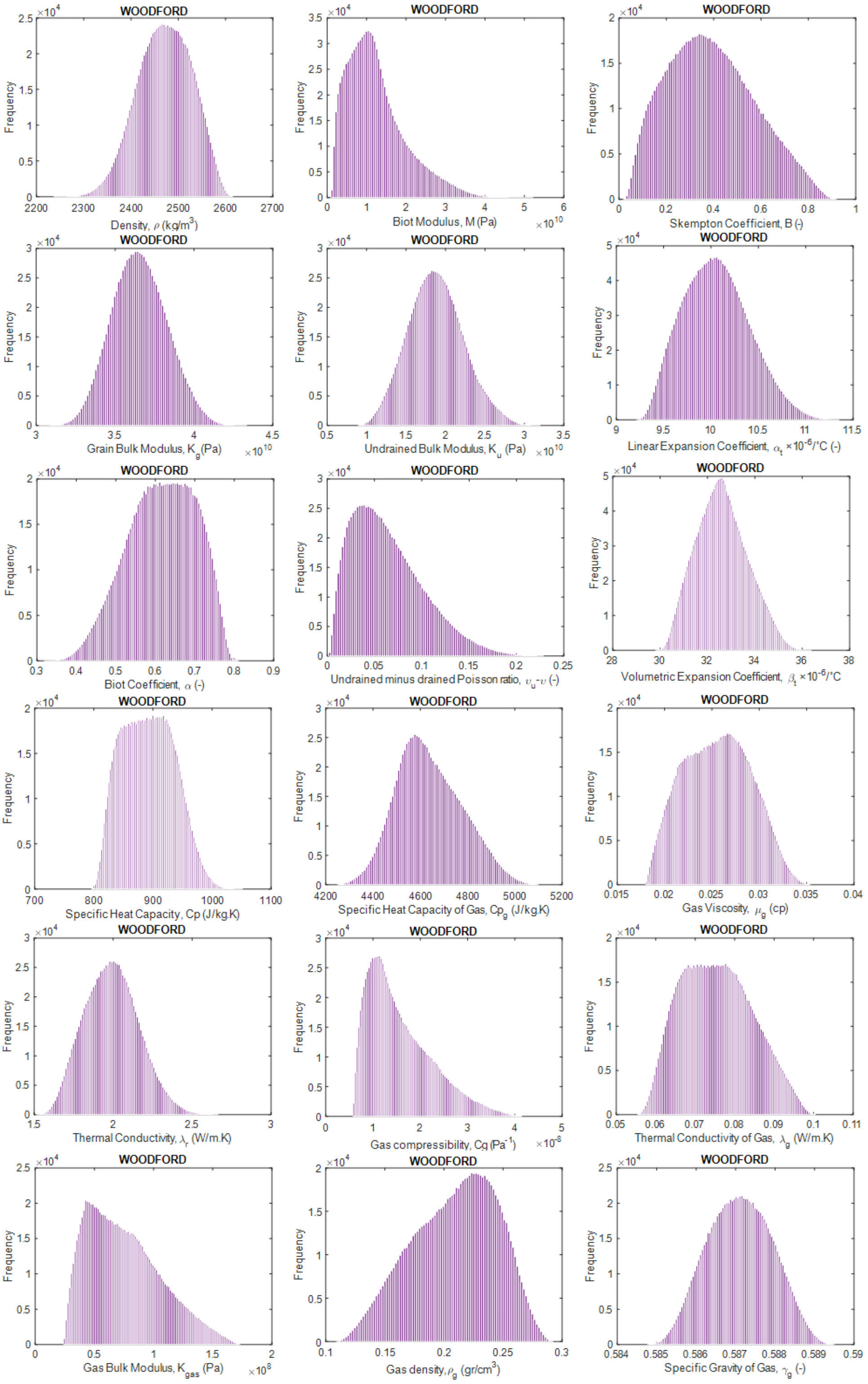

Appendix F. Distribution curves for porothermomechanical properties of Barnett shale

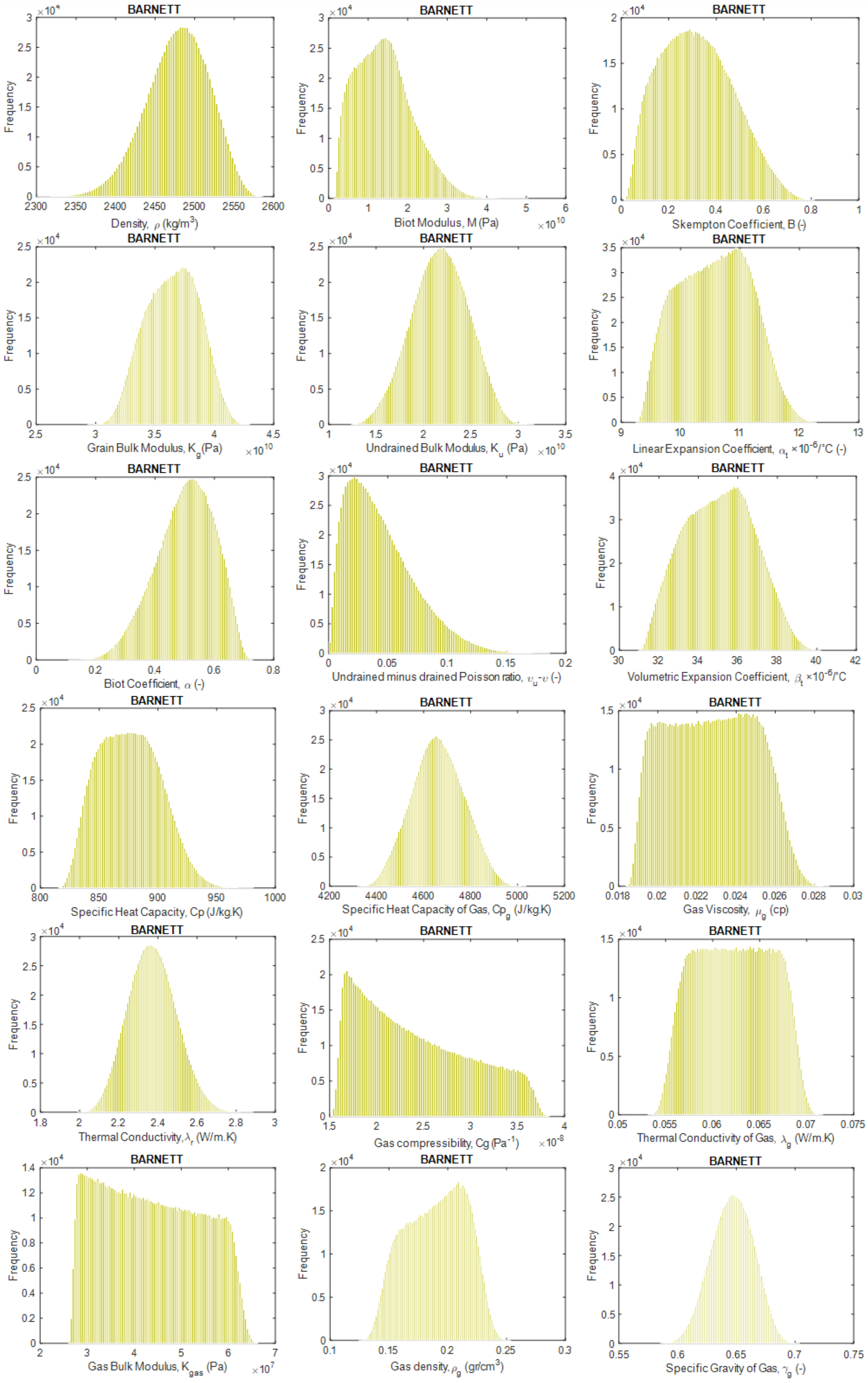

Appendix G. Distribution curves for porothermomechanical properties of Haynesville shale

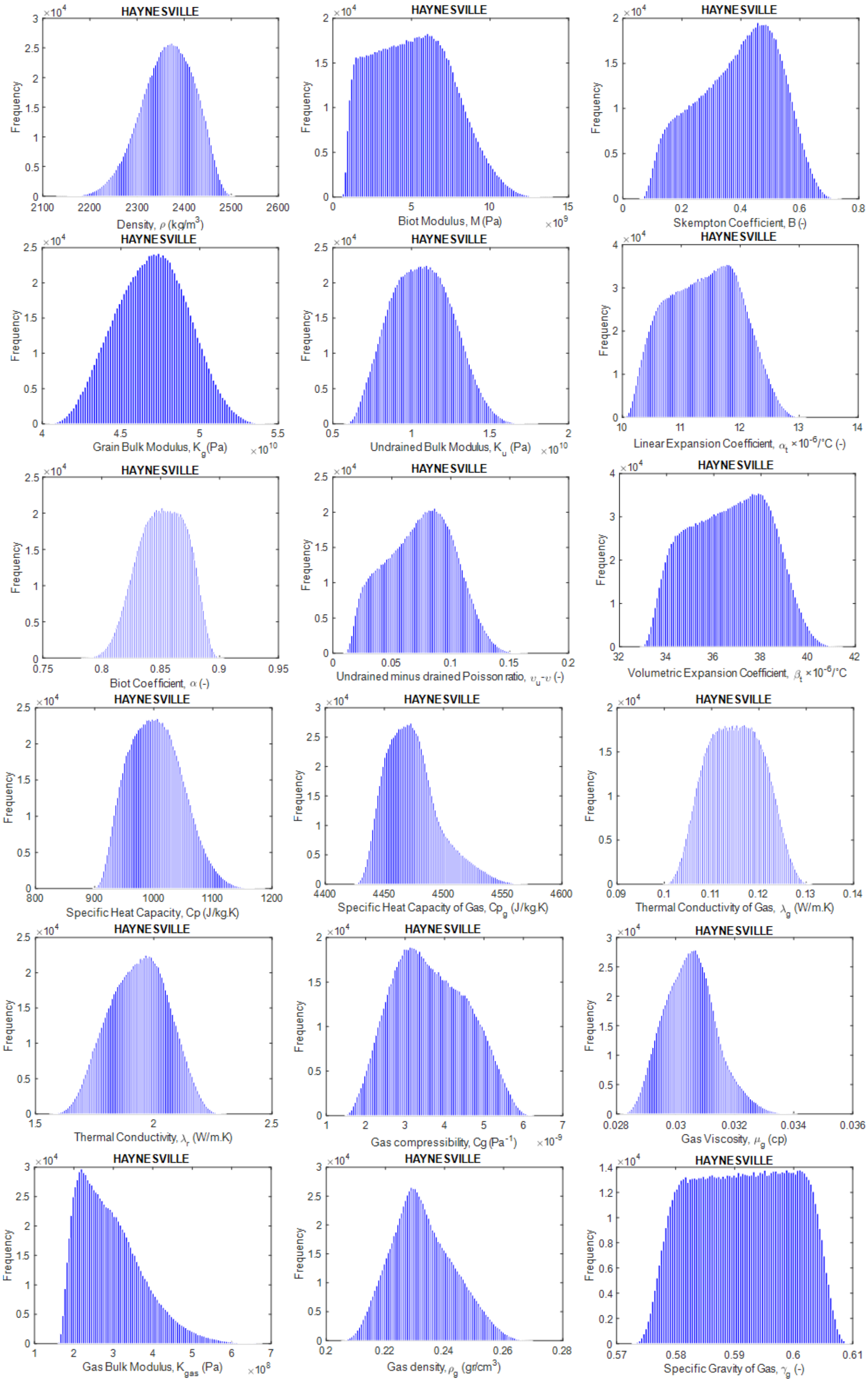

Appendix H. Distribution curves for porothermomechanical properties of Eagle Ford shale

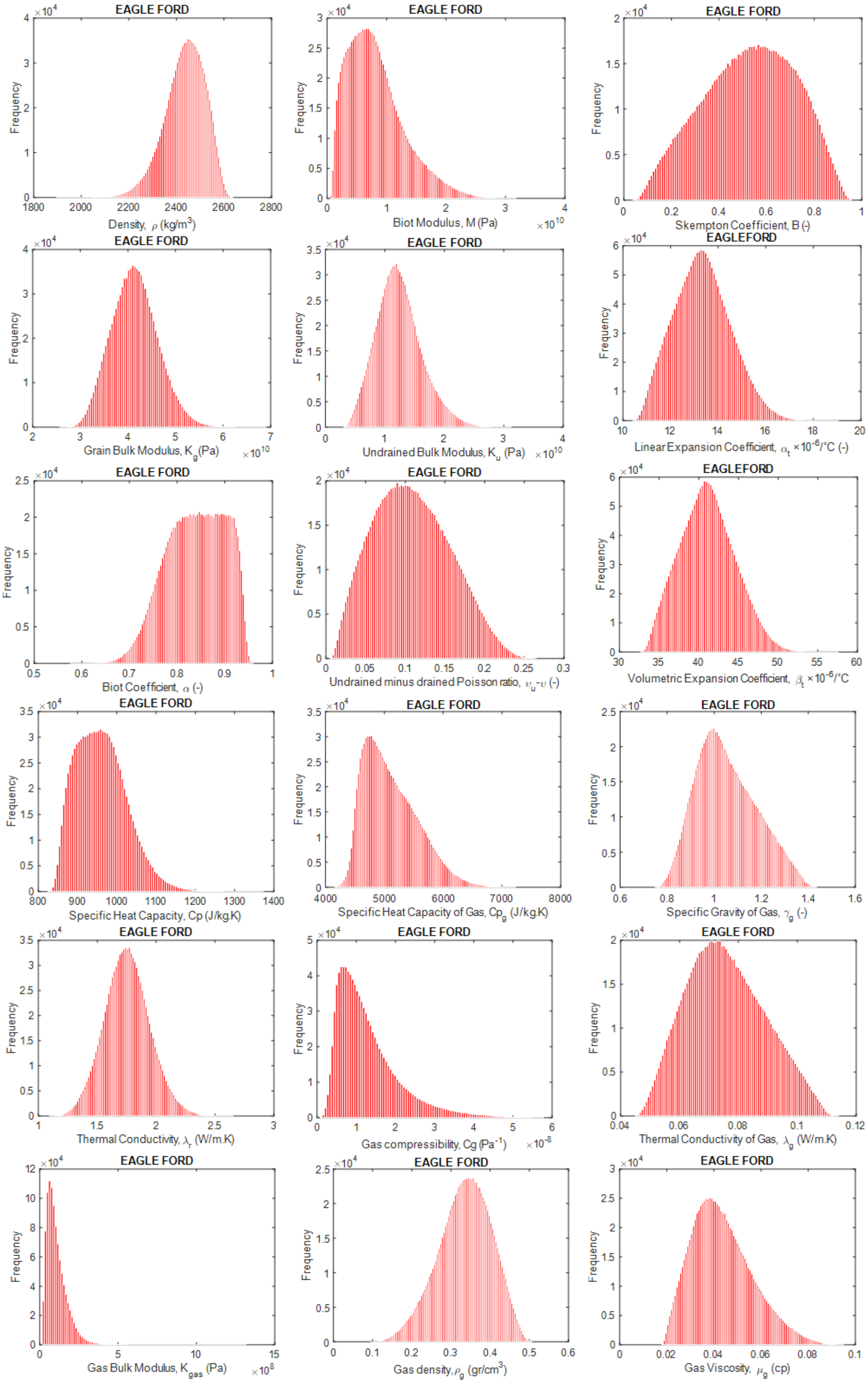

Appendix I. Distribution curves for porothermomechanical properties of Bakken shale